

CERN-PH-EP-2015-171
01 July 2015

Event shape engineering for inclusive spectra and elliptic flow in Pb–Pb collisions at $\sqrt{s_{NN}} = 2.76$ TeV

ALICE Collaboration*

Abstract

We report on results obtained with the Event Shape Engineering technique applied to Pb–Pb collisions at $\sqrt{s_{NN}} = 2.76$ TeV. By selecting events in the same centrality interval, but with very different average flow, different initial state conditions can be studied. We find the effect of the event-shape selection on the elliptic flow coefficient v_2 to be almost independent of transverse momentum p_T , as expected if this effect is due to fluctuations in the initial geometry of the system. Charged hadron, pion, kaon, and proton transverse momentum distributions are found to be harder in events with higher-than-average elliptic flow, indicating an interplay between radial and elliptic flow.

arXiv:1507.06194v1 [nucl-ex] 22 Jul 2015

© 2015 CERN for the benefit of the ALICE Collaboration.

Reproduction of this article or parts of it is allowed as specified in the CC-BY-4.0 license.

*See Appendix A for the list of collaboration members

1 Introduction

Results from Lattice Quantum Chromo-Dynamics [1, 2] predict the existence of a plasma of deconfined quarks and gluons, known as the “Quark Gluon Plasma” (QGP). This state of matter can be produced in the laboratory by colliding heavy nuclei at relativistic energies [3, 4, 5]. The QGP was found to behave as a nearly perfect liquid and its properties can be described using relativistic hydrodynamics (for a recent review, see [6]). The current experimental heavy-ion programs at Brookhaven’s Relativistic Heavy Ion Collider (RHIC) and at CERN’s Large Hadron Collider (LHC) are aimed at a precise characterization of the QGP, in particular of its transport properties.

The system created in a heavy-ion collision expands and hence cools down, ultimately undergoing a phase transition to a hadron gas, which then decouples to the free-streaming particles detected in the experiments [6]. A precision study of the QGP properties requires a detailed understanding of this expansion process. If the initial geometry of the interaction region is not azimuthally symmetric, a hydrodynamic evolution of a nearly-ideal liquid (i.e. with a small value of the shear viscosity over entropy ratio η/s) gives rise to an azimuthally anisotropic distribution in momentum space for the produced particles. This anisotropy can be characterized in terms of the Fourier coefficients v_n of the particle azimuthal distribution [7]. The shape of the azimuthal distribution, and hence the values of these Fourier coefficients, depend on the initial conditions and on the expansion dynamics. The geometry of the initial state fluctuates event-by-event and measurements of the resulting v_n fluctuations pose stringent constraints on initial state models. A quantitative understanding of the initial geometry of the produced system is therefore of primary importance [6]. A number of different experimental measurements and techniques have been proposed to disentangle the effects of the initial conditions from QGP transport, including measurements of correlations of different harmonics [8], event-by-event flow fluctuations [9, 10, 11, 12] and studies in ultra-central collisions [13, 14]. Recent results from pp and p–Pb collisions at the LHC, moreover, suggest that hydrodynamic models may be also applicable to small systems [15, 16, 17, 18, 19]. This further highlights the importance of studying Pb–Pb collisions with more differential probes, to investigate the interplay between the initial conditions and the evolution, in the system where the hydrodynamic models are expected to be most applicable.

One of the new tools for the study of the dynamics of heavy-ion collisions is the “Event Shape Engineering” (ESE) [20]. This technique is based on the observation that the event-by-event variation of the anisotropic flow coefficient (v_n) at fixed centrality is very large [12]. Hydrodynamic calculations show that the response of the system to the initial spatial anisotropy is essentially linear for the second and third harmonic, meaning that the final state v_2 (and v_3) are very well correlated with the second (and third) order eccentricities in the initial state for small values of η/s [7, 21, 22]. These observations suggest a possibility to select events in heavy-ion collisions based on the initial (geometrical) shape, providing new opportunities to study the dynamics of the system evolution and the role of the initial conditions.

The ESE technique is proposed to study ensemble-averaged observables (such as v_2 and inclusive particle spectra) in a class of events corresponding to the same collision centrality, but different v_n values. In this paper events are selected based on the magnitude of the second order reduced flow vector q_2 (see Sect. 3.1). The technique was recently applied to study correlations between different flow harmonics in the ATLAS experiment [23]. In this paper we present the results on elliptic flow and charged particle spectra in Pb–Pb collisions at $\sqrt{s_{\text{NN}}} = 2.76$ TeV obtained with ESE technique. The events selected with the ESE technique are characterized by the measurement of v_2 , to quantify the effect of the selection on the global properties of the event. In order to search for a connection between elliptic and radial flow the effect of the ESE selection on the inclusive transverse momentum distribution of charged hadrons, pions, kaons and protons is then studied. The results are presented for primary charged particles, defined as all prompt particles produced in the collision including all decay products, except those from weak decays of light flavor hadrons and of muons. The differential measurement described in this work could provide important constraints to identify the correct model for initial conditions and for the determination

of transport properties. The development of flow in hydrodynamical models is driven by the pressure gradients and anisotropy in the initial state. A correlation between anisotropic and radial flow may stem from the specific fluctuation pattern in the initial state and/or can be produced in the final state depending on the bulk and shear viscosity of the system [7].

A few important caveats, which can affect the selectivity of the ESE technique, have to be kept in mind in this study. First, the discriminating power of the q_2 selection depends on the multiplicity and v_2 value in the pseudorapidity, η , region where it is computed and on the intrinsic resolution of the detector used for the measurement. Second, non-flow effects (such as resonance decays, jets, etc. [22]) could bias the q_2 measurement. In this work we discuss both aspects in detail, making use of different detectors with different intrinsic resolution and different η coverage.

The paper is organized as follows. In Sect. 2 a brief review of the ALICE detector and of the data sample is presented. In Sect. 3 the analysis technique, with an emphasis on the event selection and on the particle identification strategy, is discussed. The results are presented in Sect. 4. Their implication for the hydrodynamic interpretation is discussed in Sect. 5. Finally, we come to our conclusions in Sect. 6.

2 ALICE detector and data sample

The ALICE detector at the CERN LHC was designed to study mainly high-energy Pb–Pb collisions. It is composed of a central barrel ($|\eta| \lesssim 0.8$ for full-length tracks), containing the main tracking and particle identification detectors, complemented by forward detectors for specific purposes (trigger, multiplicity measurement, centrality determination, muon tracking). A detailed description of the apparatus can be found in [24]. The main detectors used for the analysis presented in this paper are discussed below.

The main tracking devices in the central barrel are the Inner Tracking System (ITS) and the Time Projection Chamber (TPC). They are immersed in a 0.5 T solenoidal field. The ITS is the detector closest to the interaction point. It is a six-layer silicon tracker with a very low material budget ($\sim 7\%$ of one radiation length X_0). The ITS provides information on the primary interaction vertex and is used to track particles close to the interaction point, with the first layer positioned at a radial distance of 3.9 cm from the interaction point and the sixth one at 43 cm. It can measure the transverse impact parameter (DCA_{xy}) of tracks with a resolution of about 300 (40) μm , for transverse momentum $p_T = 0.1$ (4) GeV/c , allowing the contamination from secondary particles to be significantly reduced. The TPC [25] is a large-volume gas detector (external diameter 5 m) which measures up to 159 space points per track, providing excellent tracking performance and momentum resolution ($\sigma_{p_T}/p_T \sim 6\%$ at $p_T = 10 \text{ GeV}/c$) [26]. It is also used in this work to identify particles through the measurement of the specific energy loss, dE/dx . The dE/dx , computed as a truncated mean utilizing only 60% of the available samples, has a resolution of $\sim 5\%$ in peripheral and $\sim 6.5\%$ in central collisions [26]. At a radius of 3.7 m from the beam axis, the Time of Flight (TOF) detector measures the arrival time of particles with a total resolution of about 85 ps in Pb–Pb collisions, allowing a π/K (K/p) 2σ separation up to $p_T = 3$ (5) GeV/c . The ALICE reconstruction software performs tracking based either on the information from the TPC alone (TPC-only tracks) or on the combined information from the ITS and TPC (global tracks). The former have the advantage of an essentially flat azimuthal acceptance, and are used for v_2 and q_2 measurements. The latter provides better quality tracks ($\sigma_{p_T}/p_T = 1.5\%$ at $p_T = 10 \text{ GeV}/c$) [26], rejecting most of the secondary tracks. However, the acceptance and reconstruction efficiency of global tracks are not flat in azimuth and as a function of transverse momentum, mostly due to missing or inefficient regions of the ITS. These tracks are used for the p_T distribution measurements. TPC-only tracks can be constrained to the primary vertex (reconstructed also using the ITS information) to provide better momentum resolution.

The data used for this analysis were collected in 2010, during the first Pb–Pb run at the LHC, at a center-of-mass energy $\sqrt{s_{\text{NN}}} = 2.76$ TeV. The interaction rate was of the order of 100 Hz, low enough to avoid any space charge distortion effects in the TPC [27]. In order to check for this effect it was verified that the

results are not sensitive to the instantaneous luminosity. The trigger was provided by the V0 detector [28], a pair of forward scintillator hodoscopes placed on either side of the interaction region, covering the pseudorapidity regions $2.8 < \eta < 5.1$ (V0A) and $-3.7 < \eta < -1.7$ (V0C). Events were requested to have a signal in both sides of the V0, selecting roughly 0–90% most central collisions [29]. The V0 measures a signal whose average amplitude is proportional to the multiplicity of charged particles. The V0 acceptance times detection efficiency is approximately 90% and flat as a function of the particle p_{T} , with only a small reduction to about 85% for $p_{\text{T}} < 300$ MeV/ c . Events are further selected offline using the timing information from the V0 and from a set of two forward Zero Degree Calorimeters (ZDCs), in order to reject contamination from beam-induced backgrounds (see [29, 30, 31] for a detailed discussion). After all selections, the event sample used in the analysis consists of about 16 million events.

3 Analysis technique

3.1 Centrality and the event shape selection

The events which pass the basic selection described in Sect. 2 are divided in centrality classes based on the signal amplitude (proportional to the charged particle multiplicity) measured in the V0 detector, as described in [29]. Events in each centrality class are further subdivided into groups with different average elliptic event shapes based on the magnitude of the second order reduced flow vector q_2 [22] given as

$$q_2 = \frac{|\mathcal{Q}_2|}{\sqrt{M}}, \quad (1)$$

where M is the multiplicity and $|\mathcal{Q}_2| = \sqrt{Q_{2,x}^2 + Q_{2,y}^2}$ is the magnitude of the second order flow vector.

In this paper, the flow vector \mathcal{Q}_2 is calculated using the TPC or V0 detectors. In the TPC, tracks in the range $0.2 < p_{\text{T}} < 20$ GeV/ c and $|\eta| < 0.4$ (to avoid an overlap with the η region used for the v_2 and p_{T} distribution measurements) are used to measure

$$Q_{2,x} = \sum_{i=1}^M \cos 2\varphi_i, \quad Q_{2,y} = \sum_{i=1}^M \sin 2\varphi_i, \quad (2)$$

where φ_i is the azimuthal angle of the i -th particle and M is the number of tracks in an event.

In the forward rapidity region the V0 is used. This detector segmented into four rings, each consisting of 8 azimuthal sectors, the flow vector is hence calculated as

$$Q_{2,x} = \sum_{i=1}^{32} w_i \cos 2\varphi_i, \quad Q_{2,y} = \sum_{i=1}^{32} w_i \sin 2\varphi_i, \quad M = \sum_{i=1}^{32} w_i, \quad (3)$$

where the sum runs over all 32 channels, φ_i is the angle of the center of the sector containing channel i , w_i is the amplitude measured in channel i and M is in this case the sum of the amplitudes measured in each channel.

The discriminating power of q_2 depends on the magnitude of elliptic flow as well as on the track multiplicity used in the q_2 calculation and on the performance of the detector, including the angular resolution or the linearity of the response to the charged particle multiplicity. The good resolution of the TPC and the large multiplicity at midrapidity are used to maximize the selectivity on q_2 . However, the ALICE central barrel acceptance enables only limited separation in pseudorapidity between the region used to calculate q_2 and the region used to calculate the observables ($|\Delta\eta| = 0.1$). This separation is introduced in order to suppress unwanted non-flow correlations, which typically involve only a few particles and are in general short-range. In order to further assess the contribution of non-flow correlations, the flow vector is also calculated using the V0 detectors. This leads to a separation of more than one unit in pseudorapidity between the two regions.

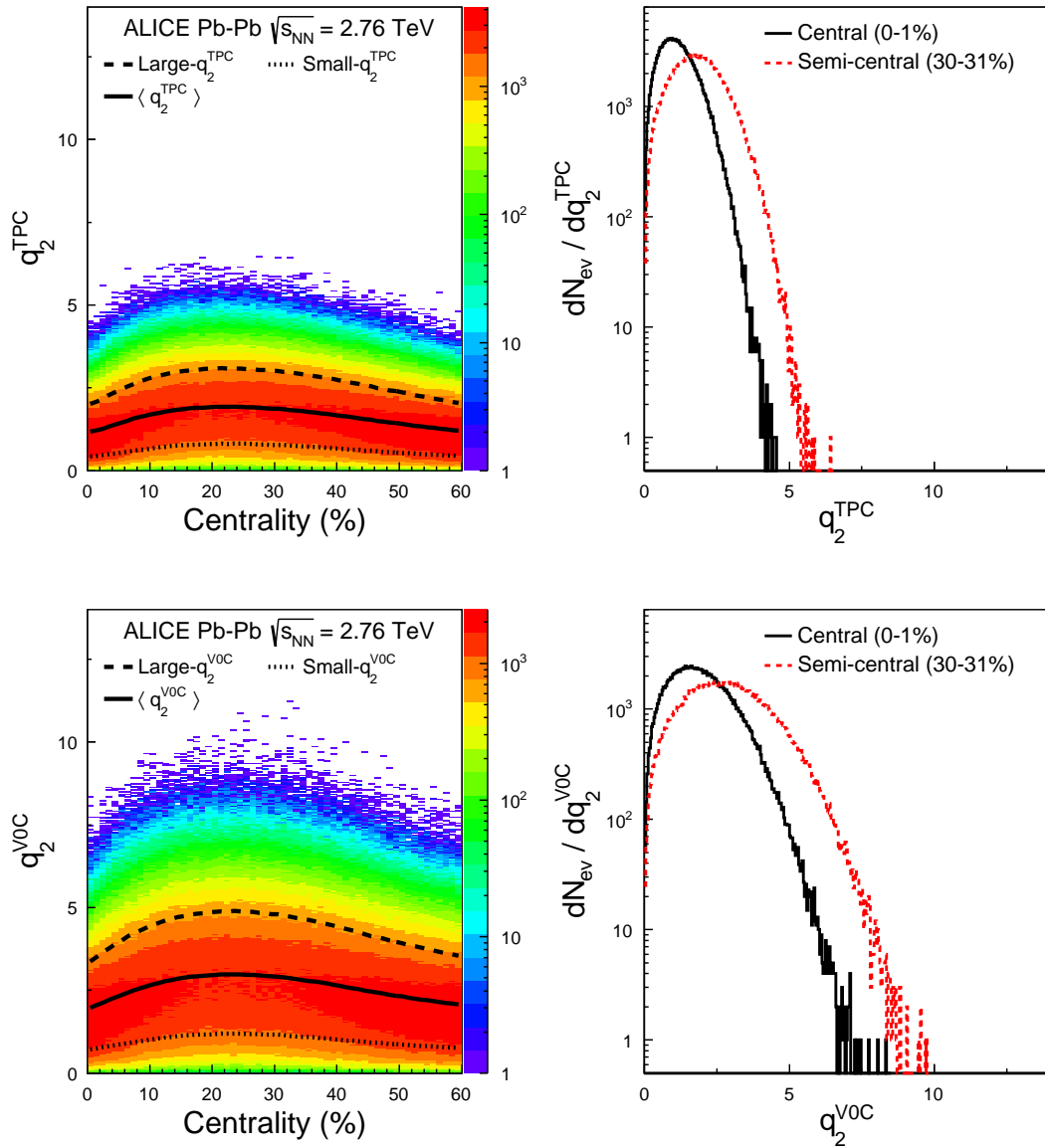


Fig. 1: Distributions of q_2^{TPC} (top) and q_2^{VOC} (bottom) as a function of centrality (left) and projections for two centrality classes, 0–1% and 30–31% (right). In each of the left panels the solid curve shows the average q_2 as a function of centrality, while the dashed and the dotted curves indicate the top 10% and the bottom 10%, respectively.

In absence of correlations, the average length of \mathcal{Q}_2 grows as \sqrt{M} [22]: q_2 is introduced to remove this trivial part of the multiplicity dependence. In case of non-zero correlations (due to either collective flow or non-flow correlations), q_2 depends on multiplicity and on the strength of the flow as [32, 22]

$$\langle q_2^2 \rangle \simeq 1 + \langle (M-1) \rangle \langle (v_2^2 + \delta_2) \rangle, \quad (4)$$

where the parameter δ_2 accounts for non-flow correlations, and the angular brackets denote the average over all events.

In the case when the multiplicity is measured via the signal amplitude in the V0 detector, the first term in Eq. 4 (unity) has to be substituted by $\langle e_i^2 \rangle / \langle e_i \rangle^2$, where e_i is the energy deposition of a single particle i . The fluctuations in e_i lead to an increase in the flow vector length and reduce the corresponding event plane resolution.

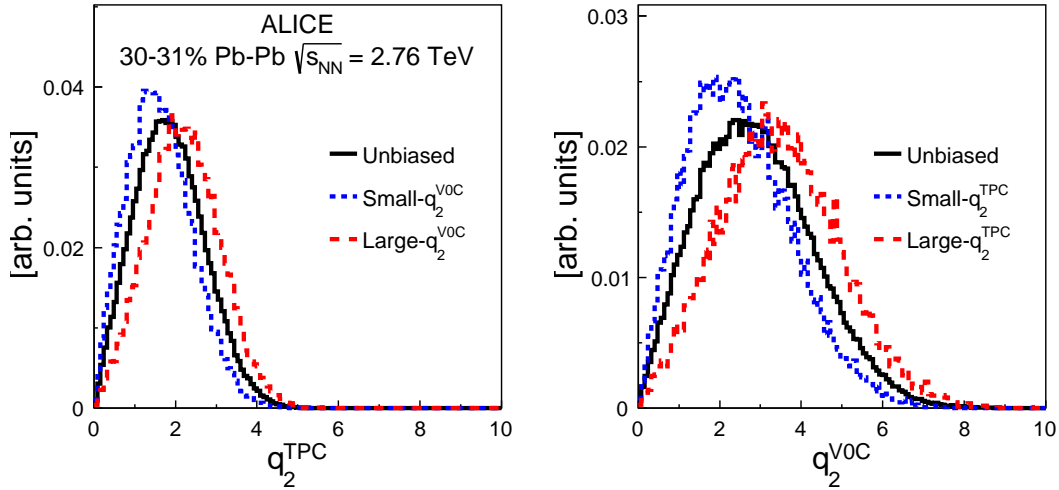


Fig. 2: Effect of the q_2^{VOC} (q_2^{TPC}) event shape selection on the q_2^{TPC} (q_2^{VOC}) distributions for events in the 30-31% centrality class.

The q_2 distribution measured with the TPC (q_2^{TPC}) and V0C (q_2^{VOC}) is shown in Fig. 1 as a function of centrality, and in two narrow centrality classes, 0–1% and 30–31%. As can be seen, q_2 reaches values twice as large as the mean value, as expected in case of large initial state fluctuations [20]. The q_2^{VOC} is larger than q_2^{TPC} , as the former is measured in a larger pseudorapidity window (integrating a larger multiplicity) and is sensitive to the fluctuations in e_i . Note also that the selectivity (discrimination power) of the two selection cuts is in principle different, due to the different detector resolution, and, in the case of V0C, smaller v_2 value at forward η , fluctuations in e_i and large contribution of secondary particles.

In the present analysis, the effect of the event shape engineering on v_2 and p_T distributions is studied. The average flow and particle spectra are measured in the pseudorapidity range $0.5 < |\eta| < 0.8$ in order to avoid overlap with the region used to calculate q_2^{TPC} . The V0C selection is used to estimate the contribution of non-flow correlations to the event-shape selection, since it provides a large η gap. As a further crosscheck, the analysis was also repeated using the V0A detector. The results obtained with V0A and V0C show a qualitative agreement with a better selectivity when the V0C is used (mostly due to the larger multiplicity in the acceptance of this detector and to the η dependence of the elliptic flow). We therefore report the results for events selected using q_2^{TPC} and q_2^{VOC} in this paper.

Due to the limited statistics, the analysis has to be performed in relatively wide centrality classes ($\sim 10\%$). The length of q_2 changes within such large centrality intervals (Fig. 1), and a cut at a fixed value of q_2 would introduce a dependence on the multiplicity that would obscure the effect of the event-shape selection. The q_2 selection is therefore evaluated in narrow (1%-wide) centrality classes. The results presented in the next sections are obtained in two event-shape classes, corresponding to the 10% of the events having the top (bottom) value of the q_2 in narrow (1% wide) slice of centrality. In the following, we refer to these two classes as “large- q_2 ” (90-100%) and “small- q_2 ” (0-10%) or, generically, as ESE-selected events. Conversely, we refer to the totality of data within a given centrality class as the “unbiased” sample.

The correlation between q_2^{TPC} and q_2^{VOC} is illustrated for events in the 30-31% centrality class in Fig. 2. The left (right) panel shows the distribution of q_2 measured with the TPC (V0C) for all events and for events in the large- q_2 and small- q_2 classes, selected with the V0C (TPC). The average q_2 changes by about 18% and 14% in the large- q_2 and small- q_2 samples respectively. In order to control the effect of fluctuations in a given detector the detailed comparison of the results obtained with q_2^{TPC} and q_2^{VOC} is crucial, as discussed in detail below. In order to disentangle the effect of the η gap and of the q_2 cut, the selection on q_2^{TPC} is also adjusted such that the average flow measured at mid-rapidity is similar to the

one in the large- q_2 sample (Sect. 4).

The ESE becomes less selective in peripheral events regardless of the detector used to compute q_2 , due to the low multiplicity. This limits the present analysis to the 60% most central events.

Space charge distortion effects in the TPC, which accumulate over many events could, in principle, bias the q_2 selection. In order to check for this and other possible instrumental effects it was verified that the results are not sensitive to the instantaneous luminosity.

3.2 Elliptic flow measurement

The elliptic flow, v_2 , is measured in the pseudorapidity range $0.5 < |\eta| < 0.8$ using the Scalar Product (SP) method [22], according to:

$$v_2\{\text{SP}\} = \frac{\langle \mathbf{u}_{2,k} \mathbf{Q}_2^* / M \rangle}{\sqrt{\mathbf{Q}_2^A \mathbf{Q}_2^{B*} / M^A M^B}} \quad (5)$$

where $\mathbf{u}_{2,k} = \exp(i2\phi_k)$ is the particle's unit flow vector, ϕ_k is the azimuthal angle of the k -th particle of interest, \mathbf{Q}_2 is the flow vector and M is the multiplicity. The full event is divided in two independent sub-events, labeled as A and B , covering two different pseudorapidity ranges, $0.5 < \eta < 0.8$ and $-0.8 < \eta < -0.5$. The particle's unit flow vector $\mathbf{u}_{2,k}$ is evaluated in the sub-event A while the flow vector \mathbf{Q}_2 and the multiplicity M in the sub-event B and vice-versa, ensuring a pseudorapidity gap of $|\Delta\eta| > 1$ between the particle of interest and the reference charged particles, which suppresses the non-flow contribution in the calculation of $v_2\{\text{SP}\}$. A flat acceptance in azimuth is achieved in this analysis selecting TPC-only tracks, constrained to the primary vertex. Tracks are required to have at least 70 clusters and a $\langle \chi^2 \rangle \leq 4$ per TPC cluster (two degrees of freedom). Tracks with a transverse distance of closest approach to the vertex (computed before constraining tracks to the primary vertex) $\text{DCA}_{xy} > 2.4$ cm or a longitudinal distance of closest approach $\text{DCA}_z > 3.2$ cm are rejected to reduce the contamination from secondary tracks. The effect of secondary particles is corrected applying the same analysis procedure to Monte Carlo events, simulated with the AMPT event generator [33] and propagated through a GEANT3 [34] model of the detector. The $v_2\{\text{SP}\}$ computed using reconstructed tracks is then compared with the one computed with generated primary particles, and the difference ($< 5\%$) is used as a correction factor.

The uncertainty on the tracking efficiency was assessed with different track samples and selections: using a set of hybrid tracks, built from a combination of global and TPC only tracks to obtain a uniform azimuthal acceptance [35], using TPC only tracks not constrained to the primary vertex, varying the minimum number of TPC clusters required in the analysis from 70 to 50 (*Track reconstruction* in Tab. 1 and 2) and weighting each track by the inverse of the (p_T -dependent) efficiency (*Tracking efficiency*).

The procedure used to estimate the centrality percentiles leads to a $\sim 1\%$ uncertainty in the definition of the centrality classes [29]. In order to propagate this uncertainty to the results presented in this paper, the measurement is repeated displacing the centrality percentile by 1%. For instance, the analysis in the 30-40% centrality class is repeated for the selection 30.3-40.4% (*Centrality resolution*). Moreover, tracks reconstructed at midrapidity (instead of the V0 signal) are used as the centrality estimator (*Centrality estimator*).

The correction for the effect of secondary particles mentioned above is strongly model dependent, therefore the difference between the v_2 estimated using generated AMPT particles and reconstructed tracks was used to estimate the corresponding systematic uncertainty, $\sim 3.5\%$ (0.7%) at $p_T = 0.2$ (1.5) GeV/ c (*Secondary particles*).

Moreover, the following systematic checks were considered: the dependence on the magnetic field configuration was studied analyzing separately samples of events collected with different polarities of the magnetic field (*Magnetic field*), analyzing positive and negative particles separately (*charge*) and analyzing samples of tracks produced at different vertex positions: $-10 < z_{\text{vtx}} < 0$ cm and $0 < z_{\text{vtx}} < 10$ cm

Effect	v_2	v_2 large- q_2	v_2 small- q_2
Track reconstruction	3.1% (0-20%)	3.1% (0-20%)	3.1% (0-20%)
	2.7% (20-60%)	2.7% (20-60%)	2.7% (20-60%)
	$(p_{\text{T}}=0.2 \text{ GeV}/c)$	$(p_{\text{T}}=0.2 \text{ GeV}/c)$	$(p_{\text{T}}=0.2 \text{ GeV}/c)$
	0.08% (0-20%)	0.08% (0-20%)	0.08% (0-20%)
	0.02% (20-60%)	0.02% (20-60%)	0.02% (20-60%)
	$(p_{\text{T}}=1.5 \text{ GeV}/c)$	$(p_{\text{T}}=1.5 \text{ GeV}/c)$	$(p_{\text{T}}=1.5 \text{ GeV}/c)$
Tracking efficiency	0.07%	0.35%	0.14 %
Centrality resolution	0.21%	0.35%	0.35%
Centrality estimator	0.57%	0.49%	0.57%
Secondary particles	3.56%	3.56%	3.56%
	$(p_{\text{T}} = 0.2 \text{ GeV}/c)$	$(p_{\text{T}} = 0.2 \text{ GeV}/c)$	$(p_{\text{T}} = 0.2 \text{ GeV}/c)$
	0.8%	0.8%	0.8%
	$(p_{\text{T}} = 1.5 \text{ GeV}/c)$	$(p_{\text{T}} = 1.5 \text{ GeV}/c)$	$(p_{\text{T}} = 1.5 \text{ GeV}/c)$
Magnetic field	NS	NS	NS
Charge	NS	NS	NS
Vertex	NS	NS	NS

Table 1: Summary of systematic errors on $v_2\{\text{SP}\}$ measurement. NS = not statistically significant.

Effect	v_2 large- q_2 /unbiased	v_2 small- q_2 /unbiased
Track reconstruction	0.14%	0.14%
Tracking efficiency	0.35 %	0.21%
Centrality resolution	0.14%	0.21%
Centrality estimator	0.14%	0.07%
Secondary particles	0.07%	0.35%
Magnetic Field	NS	NS
Charge	NS	NS
Vertex	NS	NS

Table 2: Summary of systematic errors on the $v_2\{\text{SP}\}$ ratios. NS = not statistically significant.

(*Vertex*). These effects are found to be not significant.

The systematic uncertainties in the v_2 measurements and in the ratios of v_2 in ESE-selected over unbiased events are summarized in Tab. 1 and 2. Only the checks and variations which are found to be statistically significant are considered in the systematic uncertainties [36]. Whenever the p_{T} dependence of the uncertainty is not negligible, values for characteristic p_{T} are given in the tables.

3.3 Transverse momentum distribution measurement

The measurement of the p_{T} distributions uses global tracks, which provide good resolution on DCA_{xy} (Sect. 2), and hence good separation of primary and secondary particles. The track selection requires at least 70 clusters in the TPC and at least 2 points in the ITS, out of which at least one must be in the first two layers, to improve the DCA_{xy} resolution. A p_{T} -dependent cut on the DCA_{xy} , corresponding to 7 times the experimental resolution on DCA_{xy} , is applied to reduce the contamination from secondary particles. Tracks with a χ^2 per point larger than 36 in the ITS and larger than 4 in the TPC are rejected. Finally, to further reduce the contamination from fake tracks, a consistency cut between the track parameters of TPC and global tracks was applied. For each reconstructed TPC track, the χ^2 -difference between the track parameters computed using only the TPC information constrained to the vertex and the associated global track is required to be less than 36 [37]. Charged tracks are studied in the pseudorapidity window

Effect	N_{ch}	π^\pm	K^\pm	p and \bar{p}
Track reconstruction	< 0.035%	0.07%	0.07%	0.07%
Tracking efficiency	0.21%	0.21%	0.21%	0.21%
Centrality resolution	0.07% ($p_{\text{T}} > 1.5$ GeV/ c)	0.07% ($p_{\text{T}} > 1.5$ GeV/ c)	0.14%	0.14%
Centrality estimator	0.35%	0.35%	0.35%	0.35%
PID	-	0.07% ($p_{\text{T}} > 1.5$ GeV/ c)	0.07%	0.07%
Secondary particles	< 0.035%	< 0.035%	< 0.035%	0.07%
Normalization	1.1%	1.1%	1.1%	1.1%
Magnetic field	NS	NS	NS	NS
Charge	< 0.035%	< 0.035%	< 0.035%	< 0.035%
Vertex	0.07%	0.07%	0.07%	0.07%

Table 3: Summary of systematic errors for the ratio of p_{T} distributions between large- q_2 and unbiased events. NS = not statistically significant.

Effect	N_{ch}	π^\pm	K^\pm	p and \bar{p}
Track reconstruction	< 0.035%	0.07%	0.07%	0.07%
Tracking efficiency	0.28%	0.28%	0.28%	0.28%
Centrality resolution	0.07% ($p_{\text{T}} > 1.5$ GeV/ c)	0.07% ($p_{\text{T}} > 1.5$ GeV/ c)	0.14%	0.14%
Centrality estimator	0.35%	0.35%	0.35%	0.35%
PID	-	0.07% ($p_{\text{T}} > 1.5$ GeV/ c)	0.07%	0.07%
Secondary particles	< 0.035%	< 0.035%	< 0.035%	0.07%
Normalization	0.6%	0.6%	0.6%	0.6%
Magnetic field	NS	NS	NS	NS
Charge	< 0.035%	< 0.035%	< 0.035%	< 0.035%
Vertex	0.07%	0.07%	0.07%	0.07%

Table 4: Summary of systematic errors for the ratio of p_{T} distributions between small- q_2 and unbiased events. NS = not statistically significant.

$0.5 < |\eta| < 0.8$, to avoid an overlap with the q_2^{TPC} calculation.

Particles are identified using the specific energy loss dE/dx in the TPC and their arrival time in the TOF. The technique is similar to the one presented in [15]. A track is identified as either a pion, a kaon or a proton based on the difference, in the detector resolution units, from the expected energy loss and/or time of flight $n\sigma_{\text{PID}}^i$ (with i being the particle identity under study). Below $p_{\text{T}} = 0.5$ GeV/ c , only the TPC information is used ($n\sigma_{\text{PID}}^i = n\sigma_{\text{TPC}}^i$). For larger p_{T} , the TPC and TOF information is combined using a geometrical mean: $n\sigma_{\text{PID}}^i = \sqrt{(n\sigma_{\text{TPC}}^i)^2 + (n\sigma_{\text{TOF}}^i)^2}$. Tracks are required to be within $3\sigma_{\text{PID}}$ of the expected value to be identified as π^\pm , K^\pm or p (\bar{p}). In the region where the $3\sigma_{\text{PID}}$ identification bands of two species overlap, the identity corresponding to the smaller $n\sigma_{\text{PID}}$ is assigned. This technique gives a good track-by-track identification in the following p_{T} ranges: $0.2 < p_{\text{T}} < 4$ GeV/ c for π^\pm , $0.3 < p_{\text{T}} < 3.2$ GeV/ c for K^\pm , $0.5 < p_{\text{T}} < 4$ GeV/ c for p (\bar{p}). The misidentification of tracks is below 4% for pions, 25% for kaons and 10% for protons in those ranges. Further discussion on the ALICE Particle Identification (PID) performance can be found in [26, 38]. The results for identified particles are provided in the pseudorapidity range $0.5 < |\eta| < 0.8$. However, in the case of the q_2^{VOC} selection the results were also studied at mid-rapidity $|y| < 0.5$. Results for positive and negative particles are consistent. In the following, “pions”, “kaons” and “protons”, as well as the symbols “ π ”, “K” and “p”, refer to the sum of particles and antiparticles.

The results for the spectra in ESE-selected events are presented in terms of ratios between the distributions measured in the large- q_2 (small- q_2) samples and the unbiased sample. The unbiased spectra have

already been reported in [37, 38]. Most of the corrections (and uncertainties) cancel out in these ratios, allowing for a precise determination of the effect due to the event-shape selection, as discussed in detail below. The measurement is mostly sensitive to effects which depend on the local track density, which are found to be small [39].

The systematic uncertainties are summarized in Tab. 3 and Tab. 4. As mentioned before, only the checks and variations which are found to be statistically significant are considered in the systematic uncertainties [36].

The systematic uncertainty related to the tracking is estimated varying the track selection cuts. Instead of the standard TPC cluster cut, at least 120 (out of 159) pad-rows hits in the TPC and a fraction of shared clusters in the TPC < 0.4 , are required (*Track reconstruction* in Tab. 3 and 4).

The possible effect of a track-density-dependent efficiency (which would influence in a different way events with the large- and small- q_2 selection) is investigated using simulations based on the AMPT event generator [33] and a parametric event generator tuned to reproduce the ALICE spectra and v_2 measurements [39]. This effect leads to an uncorrelated systematic error of about 0.2% and a normalization error of 0.4% (*Tracking efficiency*).

The uncertainty on the centrality is estimated varying the definitions of centrality classes by 1% and using tracks as the centrality estimator. These checks lead to an uncorrelated uncertainty of about 0.1% and 0.35%, respectively and a normalization uncertainty below 1% in the ratios of spectra (*Centrality resolution* and *Centrality estimator*).

The systematic effect related to the particle identification is studied performing several variations to the PID approach described above. The $n\sigma_{\text{PID}}$ cut is varied between 2 and 4. Alternatively, if a track is consistent with more than one particle assignment within the $n\sigma_{\text{PID}}$ cut, double counting is allowed. As compared to the standard strategy where only the identity closest to the measured $n\sigma_{\text{PID}}$ is selected, this approach leads to a slightly larger contamination from misidentified tracks, but also to a larger efficiency. Finally, an exclusive $n\sigma_{\text{PID}}$ strategy was used, which drastically reduces misidentification: a particle is only accepted if it is compatible with only one mass hypothesis at $3\sigma_{\text{PID}}$. As a further cross-check, a Bayesian approach [26] was also considered. This method allows for better control of contamination at high p_{T} . Overall, the uncertainty related to the particle identification strategy is less than 0.1% (*PID*).

The effect of secondary particles depends on the p_{T} distribution of weakly-decaying primary particles, and could be different for the large- and small- q_2 samples. This effect is estimated to be at most $\sim 0.1\%$ for protons with the TPC ESE selection and negligible in all other cases (*Secondary particles*).

Possible effects related to the magnetic field and to the charge state are addressed studying separately events collected with different magnet polarities (*Magnetic field*) and different charges (*Charge*), as in the case of the $v_2\{\text{SP}\}$ measurement. Particles produced at different longitudinal position cross a different portion of the detector, with different reconstruction efficiency. The samples of events produced with a negative ($-10 < z_{\text{vtx}} < 0$ cm) and positive ($0 < z_{\text{vtx}} < 10$ cm) longitudinal vertex coordinate with respect to the nominal interaction point were studied separately (*Vertex*).

4 Results

4.1 Charged particle elliptic flow

The event-shape selection is studied in Fig. 3, where the $v_2\{\text{SP}\}$ as a function of p_{T} is reported for the unbiased and ESE-selected samples, with both the q_2^{TPC} ($|\eta| < 0.4$) and q_2^{V0C} ($-3.7 < \eta < -1.7$) selections in different centrality classes. Figure 4 shows the ratio between the v_2 measured with the large- q_2 (small- q_2) selection and the unbiased sample. Selecting the 10% highest (lowest) q_2^{TPC} samples leads to a change of 30-50% in the $v_2\{\text{SP}\}$ measured, depending on centrality. The change is smaller (~ 10 -

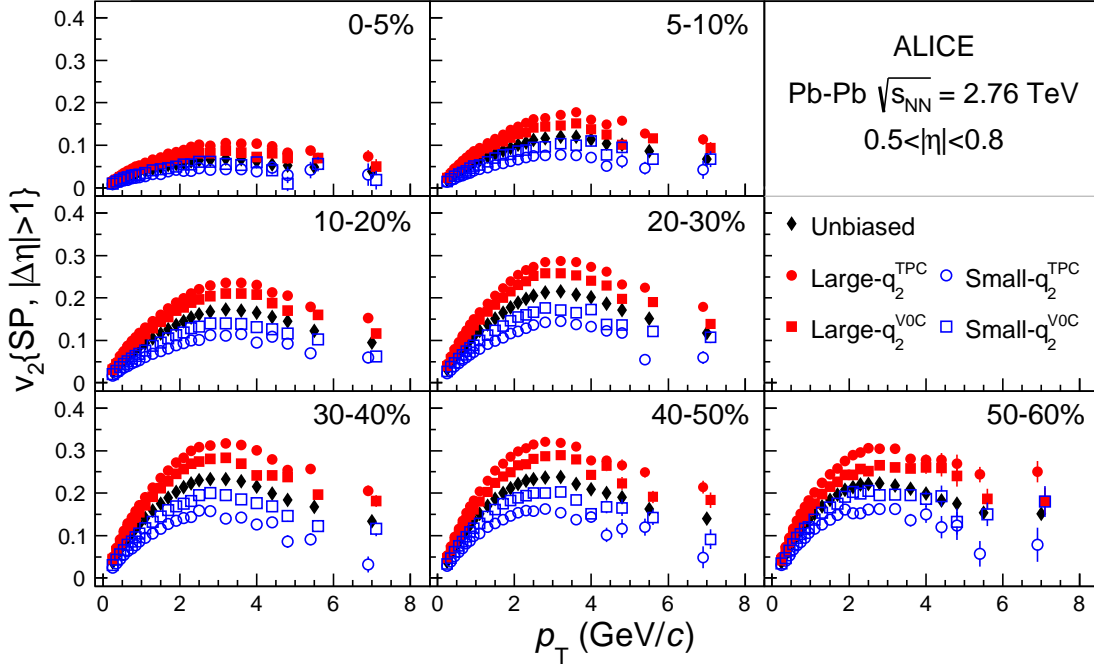


Fig. 3: Measurement of $v_2\{SP\}$ as a function of p_T in different centrality classes for the unbiased, the large- q_2 and the small- q_2 samples. Only statistical uncertainties are plotted (systematic uncertainties are smaller than the markers).

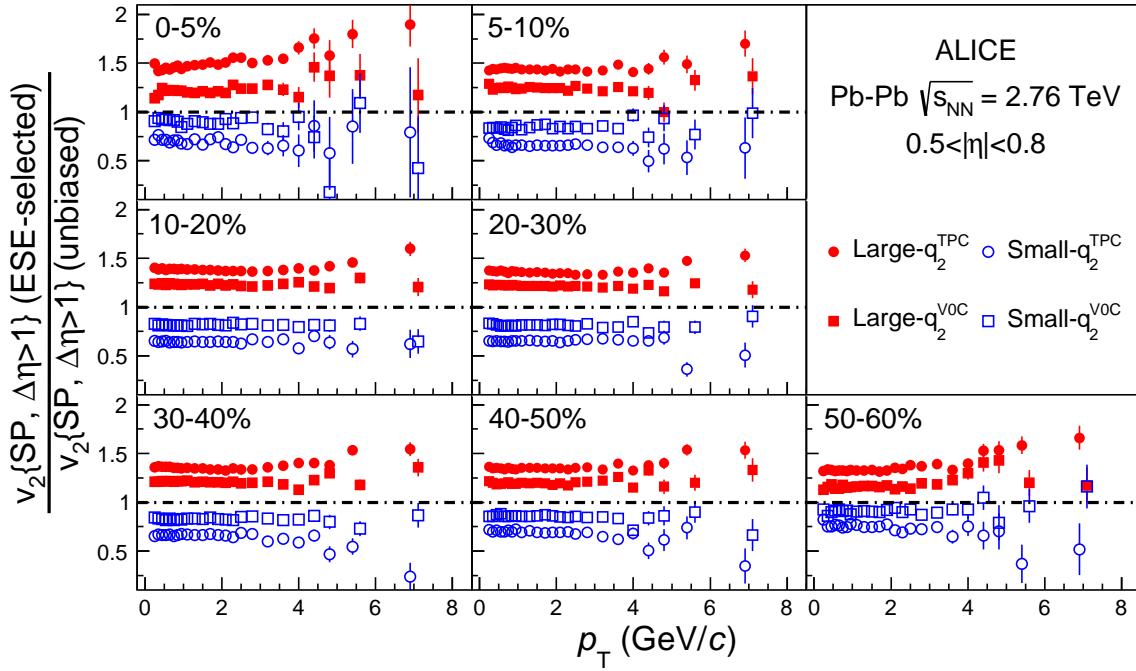


Fig. 4: Ratio of $v_2\{SP\}$ in the large- q_2 and small- q_2 samples to unbiased sample. Only statistical uncertainties are plotted (systematic uncertainties are smaller than the markers).

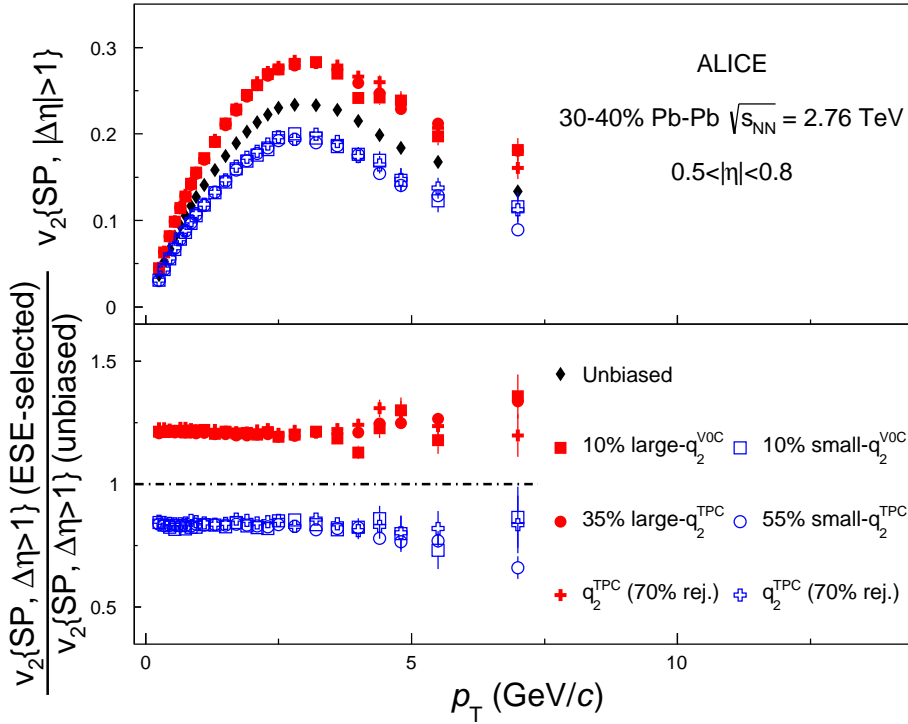


Fig. 5: Comparison between the effect of the event-shape selection obtained with the standard VOC and with the tuned TPC selections (see text for details), in the centrality class 30-40%. Top: $v_2\{\text{SP}\}$, bottom: ratios to the unbiased sample. Only statistical uncertainties are plotted (systematic uncertainties are smaller than the markers).

25%) in the case of q_2^{VOC} -based selection, as compared to the q_2^{TPC} case. As already indirectly inferred from the difference between 2nd and 4th order flow cumulants $v_2\{2\}$ and $v_2\{4\}$ in [12], the elliptic flow response of the system to geometry fluctuations is almost independent of p_T . For all centralities, the change observed in Fig. 4 depends indeed weakly on p_T , up to at least 4-5 GeV/ c . This indicates that a cut on q_2 selects a global property of the event, likely related to the initial shape in the overlap region. The only exception to the previous observation is the 0-5% centrality class, where for the q_2^{TPC} selection an increasing trend with p_T is observed. In this centrality class the mean value of v_2 is small, due to the almost isotropic shape in the initial state. Moreover, relative flow fluctuations are large in central collisions, with a p_T dependence similar to the one shown in Fig. 4 [12]. The analysis of the p_T spectra presented in Section 4.2 gives an additional insight into the trend observed in Figure 4.

For $p_T \gtrsim 4 - 5$ GeV/ c , the ratio ESE-selected/unbiased $v_2\{\text{SP}\}$ increases for the large- q_2 selection. This trend is more pronounced for the q_2^{TPC} selection and for the most central and the most peripheral classes. A fit with a constant over the full p_T range yields χ^2 per degree of freedom values in the range 2-6 (depending on centrality) for the q_2^{TPC} selection and < 2 for the q_2^{VOC} selection. Fitting the ranges $p_T < 5$ GeV/ c and $p_T > 5$ GeV/ c with two different constants indicates an increase for the large- q_2 selection of order 5% and 10% for the q_2^{VOC} and q_2^{TPC} selections, respectively. This difference could be due to a small non-flow-induced bias. At high p_T the v_2 is believed to be determined by the path-length dependence of parton energy loss [12].

The difference between the q_2^{TPC} and q_2^{VOC} can be due to the different selectivity (see Sect. 3.1), but also to a different contribution of non-flow correlations between the q_2 and the v_2 measurements. Replacing the q_2^{TPC} selection with the q_2^{VOC} one changes both non-flow and selectivity at the same time. To disentangle these two contributions, the selectivity of the q_2^{TPC} selection was artificially reduced. This is achieved

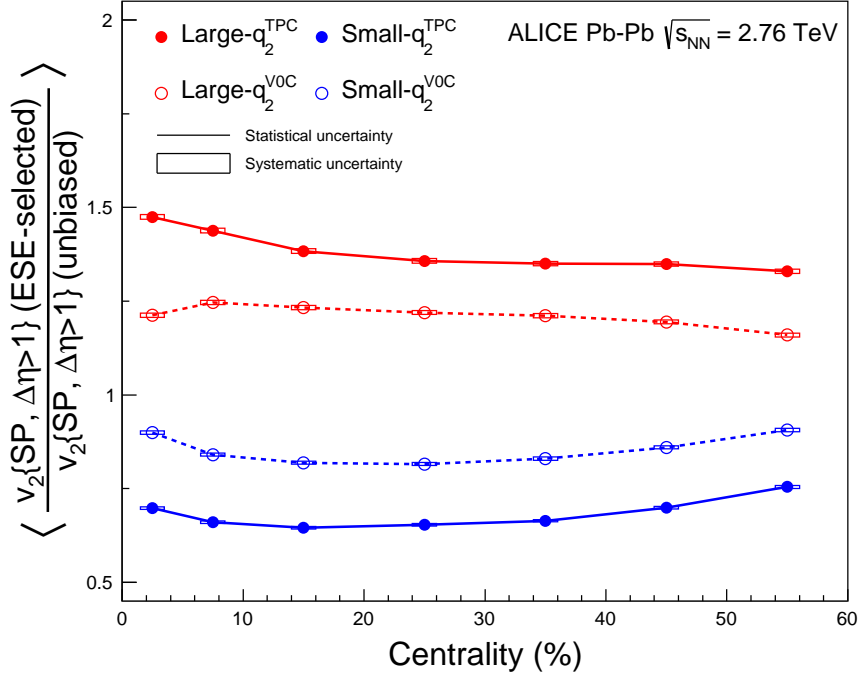


Fig. 6: Centrality dependence of the average $v_2\{\text{SP}\}$ variation in the large- q_2 and small- q_2 samples.

either relaxing the selection itself or rejecting a random fraction of tracks for the computation of q_2^{TPC} , while still selecting 10% of the events. It is found that selecting the class 65–100% for the large- q_2 sample (0–55% for the small- q_2 sample) with q_2^{TPC} , or alternatively rejecting 70% of the TPC tracks, leads to an average variation of the $v_2\{\text{SP}\}$ in the range $0.2 < p_T < 4$ GeV/ c comparable to the one obtained with the standard 10% q_2^{V0C} selection. The results are shown in Fig. 5 for the centrality class 30–40%. Not only is it possible to find a cut which leads to the same average variation in $v_2\{\text{SP}\}$, but the p_T dependence is very similar in both cases. Rejecting randomly 70% of the tracks changes the selectivity of q_2^{TPC} without affecting non-flow correlations between the q_2^{TPC} selection and $v_2\{\text{SP}\}$ measurement (as the η gap is not varied). Also in this case, it is found that the effect of the q_2 selection does not depend on p_T . A similar result, with the same value of the relaxed cut or fraction of rejected tracks, is found for the centrality interval 10–50%. Moreover, as it will be discussed in the next section, the same relaxed selections lead to the same effect on the p_T distributions.

These checks demonstrate that the selectivity of the cut is the main reason for the difference between the TPC and V0C selections. Due to the large η gap, the non-flow contribution is expected to be negligible in the case of the q_2^{V0C} selection. The agreement observed in Fig. 5 indicates that, in the centrality classes 10–50%, this is also the case for the q_2^{TPC} selection in the range $p_T < 5$ GeV/ c , a transverse momentum region dominated by hydrodynamic effects [38]. It is worth noticing that the ATLAS Collaboration measured a modification of the elliptic flow of $\sim 35\%$, nearly independent of p_T up to ~ 12 GeV/ c in the 20–30% centrality class, while measuring v_2 and q_2 with a pseudorapidity gap of 0.7 units [23]. The increasing trend in the centrality class 0–5% is also observed in [23]¹.

To study the centrality and the q_2 dependence of $v_2\{\text{SP}\}$ in ESE-selected event classes, we quantified the average change for each centrality class fitting the ratios in the range $0.2 < p_T < 4$ GeV/ c with a

¹See auxiliary figures available on the ATLAS Collaboration web page <https://atlas.web.cern.ch/Atlas/GROUPS/PHYSICS/PAPERS/HION-2014-03/>

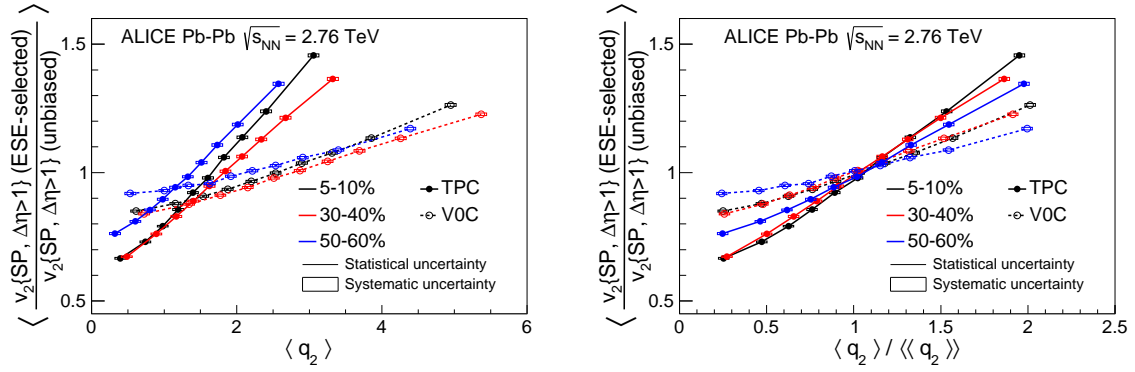


Fig. 7: Average $v_2\{\text{SP}\}$ variation as a function of the absolute (left) values and self-normalized (right) values of the q_2^{TPC} and q_2^{V0C} for several centrality classes.

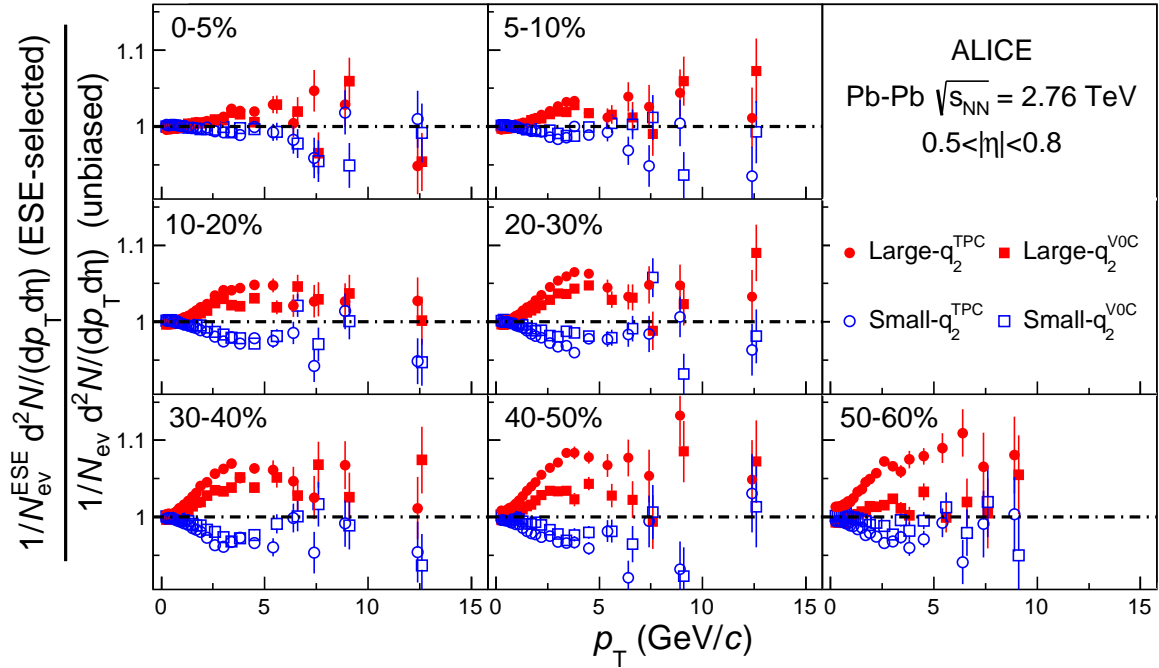


Fig. 8: Ratio of the p_T distribution of charged hadrons in the large- q_2 or small- q_2 sample to the unbiased sample (q_2^{V0C} and q_2^{TPC} selections) in different centrality classes. Only statistical uncertainties are plotted (systematic uncertainties are smaller than the markers).

constant². The centrality dependence of the average change in the large- q_2 and small- q_2 selection is reported in Fig. 6. The trend obtained with the q_2^{TPC} and q_2^{V0C} selections is very similar, except for the most central class 0–5%, where the average is influenced by the non-flat trend seen in Fig. 4. This once again reinforces the conclusion that the non-flow contamination is small also in the TPC selection case for the bulk of particles. The relative importance of non-flow changes with centrality. A large non-flow bias would therefore introduce a centrality dependence in the relative trend between the q_2^{TPC} and q_2^{V0C} selections, which is not observed. The dependence of the $v_2\{\text{SP}\}$ variation on q_2^{TPC} and q_2^{V0C} is shown for the centrality classes 5–10%, 30–40% and 50–60% in Fig. 7. The left panel shows the absolute q_2 values on the x axis, while the right panel depicts the self-normalized values, defined as the average q_2

²The result of the fit is numerically equivalent to the direct computation of the integrated v_2 in the range $0.2 < p_T < 20$ GeV/ c .

value in ESE-selected events over the average q_2 values for all events in a given centrality class. The V0C selection spans a larger range but the TPC is more selective, as is clearly seen from the different slope of the TPC and V0C curves. In both cases the average q_2 reaches values twice as large compared to those in the unbiased sample, (Fig. 7, right).

In summary, the observations reported in this section indicate that the ESE selects a global property of the collisions, as suggested by the flat modification in the v_2 as a function of p_T . The q_2^{TPC} leads to a change twice as large than the corresponding q_2^{V0C} selection. The difference between the two seems to be mostly due to the different discriminating power rather than to non-flow effects.

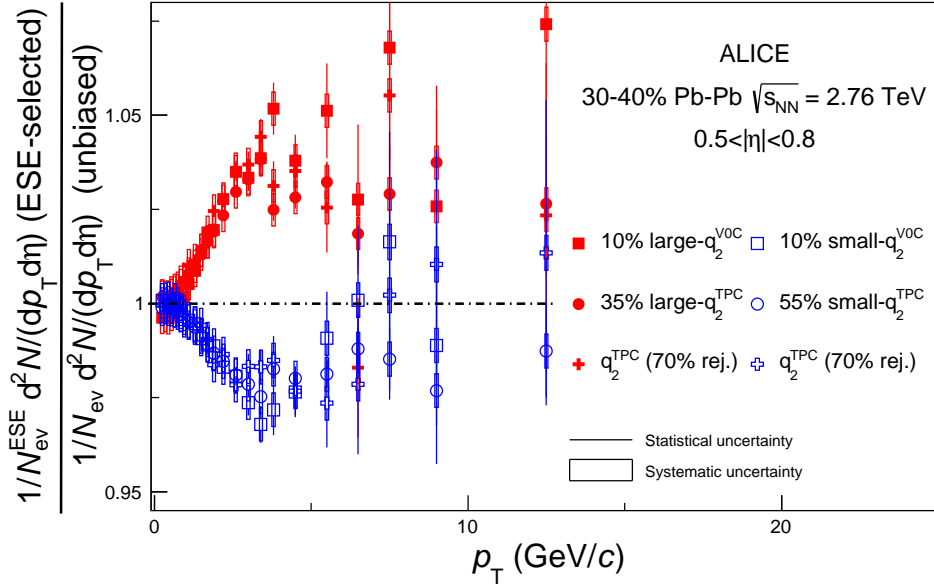


Fig. 9: Ratio of the p_T distribution of charged hadrons in the large- q_2 or small- q_2 sample to the unbiased sample. Comparison between the effect of the event-shape selection obtained with the standard V0C and with the tuned TPC selections (see text for details), in the centrality class 30-40%.

4.2 Transverse momentum distributions

In order to study the interplay between the initial configuration of the system and the dynamics of the expansion of the fireball, the effect of the ESE selection on the single particle p_T distribution is reported in Fig. 8, for the q_2^{TPC} and q_2^{V0C} selections. As discussed in Sect. 3.1 the reduced flow vector is calculated in the TPC detector in the pseudorapidity range $|\eta| < 0.4$. In order to avoid overlap between the q_2^{TPC} and p_T distribution measurements, only the region $0.5 < |\eta| < 0.8$ is used to measure the p_T distributions. This ensures at least 0.1 units of pseudorapidity separation between the q_2 and spectra measurements, thus suppressing the effect of short-range correlations. For consistency with the TPC analysis, the same pseudorapidity range is used in the case of the V0C selection. In the q_2^{V0C} case, it is also possible to study the spectra at mid-rapidity $|\eta| < 0.8$ without any overlap with the q_2 measurement. The results agree within uncertainty with those in $0.5 < |\eta| < 0.8$.

The spectra in the large- q_2 sample are harder than those in the small- q_2 one. The ratio to the unbiased spectra reaches a maximum around $p_T = 4$ GeV/c, and then stays approximately constant within large uncertainties.

The effect of the selection is more pronounced in semi-central events (~ 30 – 50%), and decreases both towards more central and more peripheral collisions. This can be understood as due to the fact that the q_2 spans a larger dynamic range in semi-central collisions (Fig. 1 and Fig. 7). In the most peripheral central-

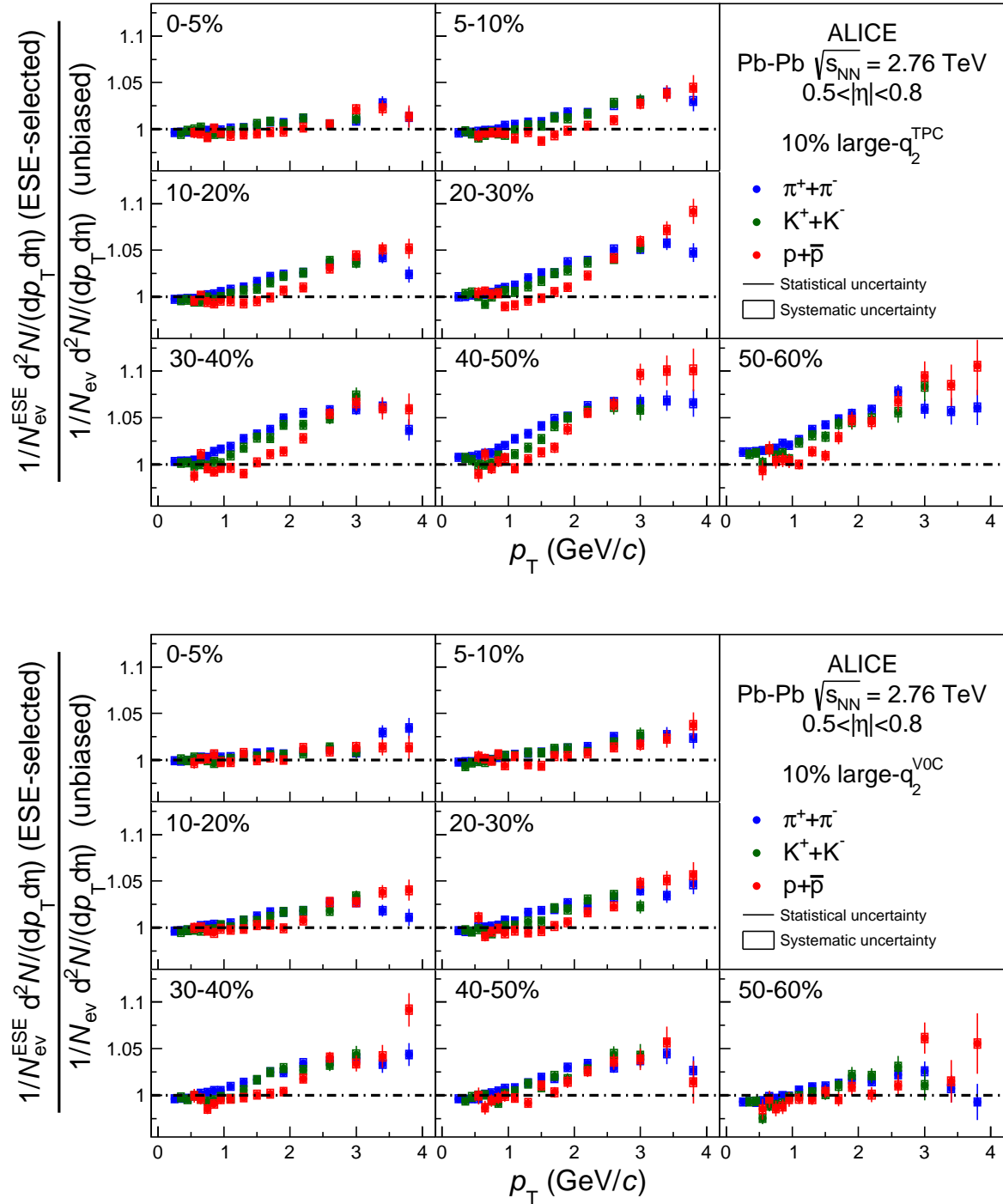


Fig. 10: Ratio of the p_T distribution of identified charged hadrons in the large- q_2 sample to the unbiased sample for the q_2^{TPC} (top) and q_2^{VOC} (bottom) selections.

ity class studied in this paper (50–60%) the effect of the TPC-based selection is still very pronounced, while the q_2^{VOC} selection is less effective. This may indicate a small contamination from non-flow effects in the most peripheral bin, consistent with observations discussed for the $v_2\{\text{SP}\}$ measurement in Sect. 4.1. In the most central class (0-5%) the modification of the spectrum is very small. This suggests that the trend observed in the same centrality class in Fig. 4 is likely to be dominated by flow fluctuations rather than non-flow contributions.

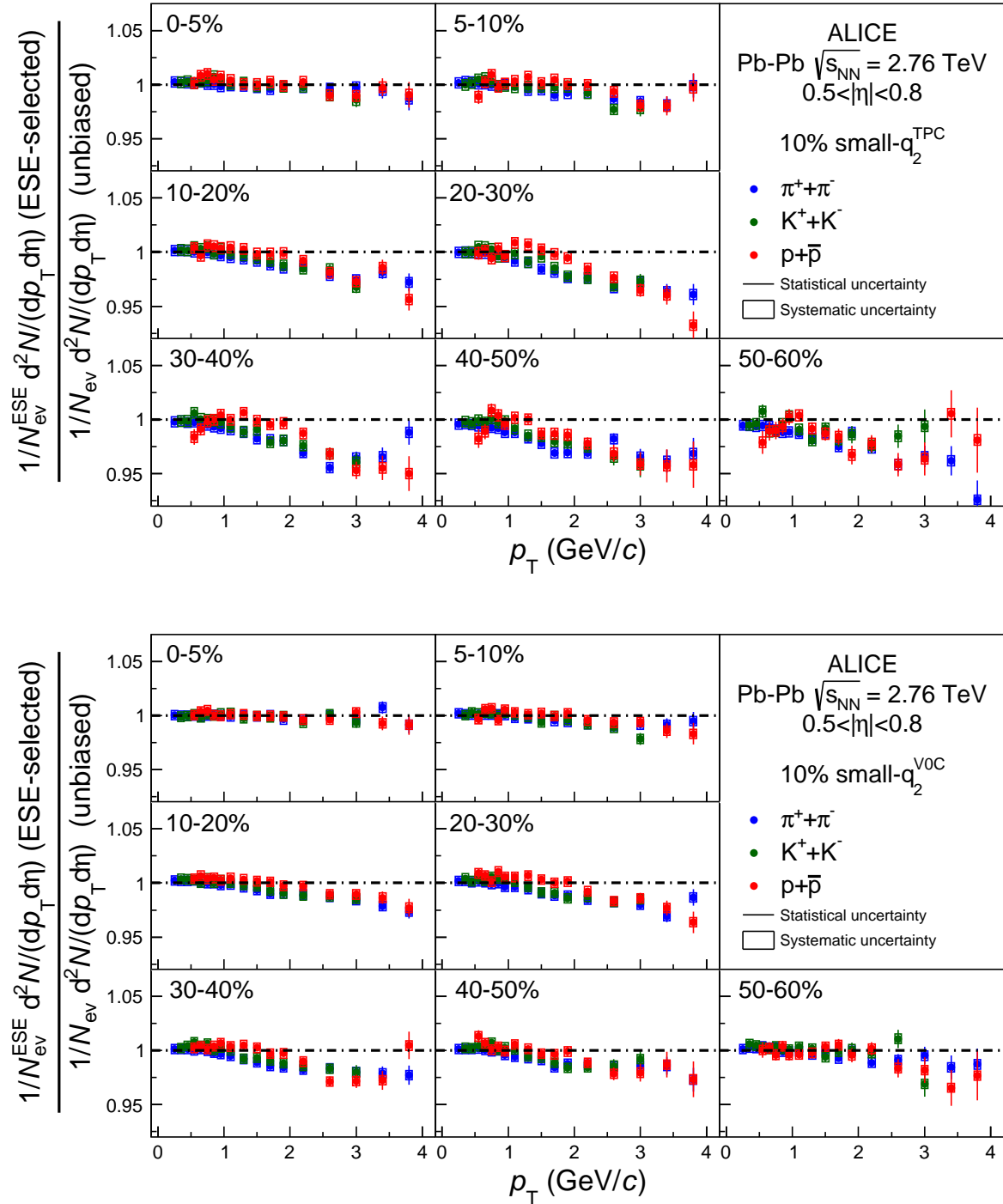


Fig. 11: Ratio of the p_T distribution of identified charged hadrons in the small- q_2 sample to the unbiased sample for the q_2^{TPC} (top) and q_2^{VOC} (bottom) selection.

As in the previous section, we disentangle the effect of non-flow and q_2 selectivity either relaxing the q_2^{TPC} selection or randomly rejecting a fraction of the tracks. The relaxed cut and the fraction of rejected tracks tuned to reproduce the v_2 variation in $0.2 < p_T < 4$ GeV/ c in Sect. 4.1 are used. Figure 9 shows that these selections yield results compatible with the standard q_2^{VOC} selection. A similar result (with the same relaxed cuts or fraction of rejected tracks) is found for all centralities up to $\sim 50\%$, after which non-flow effects seem to become relevant.

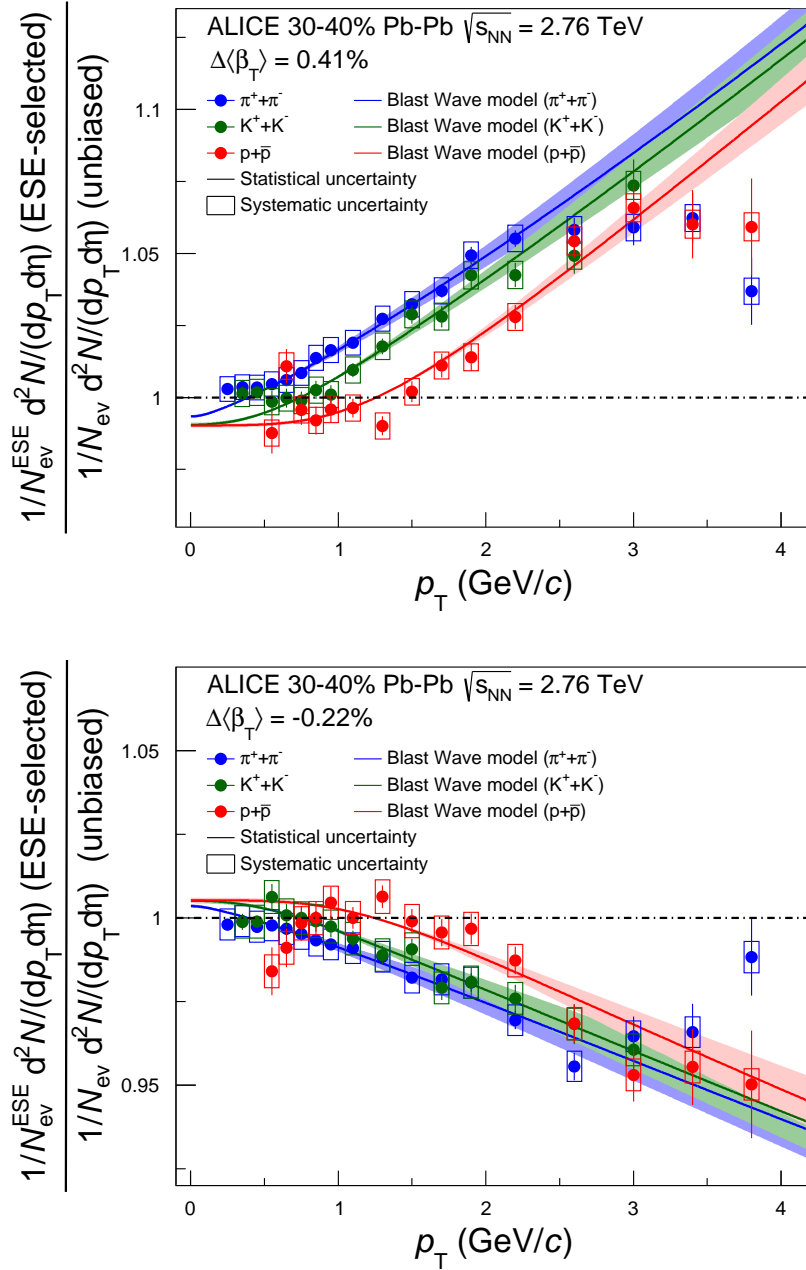


Fig. 12: Ratio of the p_T distribution of identified charged hadrons in the large- q_2 (top) and small- q_2 (bottom) sample to the unbiased sample (q_2^{TPC} selection), in 30-40% centrality class. Lines: ratio of the blast-wave parametrizations (see text for details).

As discussed in Sect. 4.1, we conclude that the effect of non-flow is small and that the main factor driving these observations is the average v_2 at mid-rapidity.

The modification on the spectra of identified π , K, and p is reported in Fig. 10 and Fig. 11 for different centrality classes. The same pattern measured in the case of non-identified hadrons is observed. Moreover, a clear mass ordering is seen: the modification is more pronounced for heavier particles. Conversely, the spectra in the small- q_2 sample are softer. In the case of the V0C selection the analysis was also repeated in the region $|y| < 0.5$, yielding consistent results.

These observations suggest that the spectra in the large- q_2 (small- q_2) sample are affected by a larger

(smaller) radial flow push. This hypothesis was tested with a blast-wave [40] study. A ratio of two blast-wave functions was used to fit the spectra ratios shown in Fig. 10 and Fig. 11. The parameters were initially fixed to the values from [38], where they were tuned to describe the inclusive spectra of pions, kaons and protons. Then, the $\langle\beta_T\rangle$ parameter of the numerator function was allowed to change (while keeping the overall integral of the function constant). The fit was performed as in [38] in the transverse momentum ranges 0.5-1 GeV/c, 0.2-1.5 GeV/c, 0.3-3 GeV/c for π , K, p, respectively. The agreement with the data is good, also outside the range used to determine the parameters, up to $p_T \sim 3$ GeV/c. The fits yield the following result for the difference $\Delta\langle\beta_T\rangle$ between the $\langle\beta_T\rangle$ parameter of the numerator and denominator function: $\Delta\langle\beta_T\rangle = (0.41 \pm 0.03)\%$ (large- q_2) and $\Delta\langle\beta_T\rangle = (-0.22 \pm 0.03)\%$ (small- q_2) for the centrality class 30-40%, as shown in Fig. 12.

5 Discussion

In this paper the first application of the Event Shape Engineering (ESE) [20] to the analysis of ALICE data was presented.

The results on the $v_2\{\text{SP}\}$ measurement suggest that the ESE technique selects a global property of the collision, likely related to the eccentricity in the initial state. The measurement of p_T spectra indicates that events with larger eccentricity show an increased radial flow. A correlation between elliptic and radial flow could be introduced either at the initial stage, due to the specific fluctuation patterns in the energy deposition, or during the hydrodynamic evolution of the system, due to an interplay of bulk and shear viscosity [7].

A Glauber Monte Carlo simulation was performed to estimate the possible correlation between the initial eccentricity and azimuthally-averaged pressure gradients. In the model, the multiplicity of charged particles in the acceptance of the V0 detector, used to determine the centrality classes, is computed following [29]. A “number of ancestors” $N_{ancestors}$ is derived from the number of participant nucleons (N_{part}) and binary collisions (N_{coll}) as

$$N_{ancestors} = fN_{part} + (1-f)N_{coll}. \quad (6)$$

Each ancestor is assumed to produce particles following a negative binomial distribution with parameters taken from [29].

The participant density, defined following [41, 42, 9, 43] as N_{part}/S , is used as a proxy for the magnitude of the pressure gradients. The average cross-sectional area S and participant eccentricity ε are computed as

$$S = 4\pi\sigma_x\sigma_y = 4\pi\sqrt{\sigma_x^2\sigma_y^2 - \sigma_{xy}^2}, \quad (7)$$

$$\varepsilon = \frac{\sigma_y^2 - \sigma_x^2}{\sigma_x^2 + \sigma_y^2} = \frac{\sqrt{(\sigma_y^2 - \sigma_x^2)^2 + 4\sigma_{xy}^2}}{\sigma_x^2 + \sigma_y^2}, \quad (8)$$

where

$$\sigma_x^2 = \langle x^2 \rangle - \langle x \rangle^2, \quad \sigma_y^2 = \langle y^2 \rangle - \langle y \rangle^2, \quad \sigma_{xy} = \langle xy \rangle - \langle x \rangle \langle y \rangle. \quad (9)$$

The unprimed coordinates are given in the fixed laboratory coordinate frame. Primed coordinates, x' and y' , are calculated in the so-called participant coordinate system, rotated with respect to the laboratory coordinate frame such that the minor symmetry axis of the participant nucleon distribution coincides with the x' direction. The normalization of the area is chosen such that for a Gaussian distribution the average density coincides with N_{part}/S .

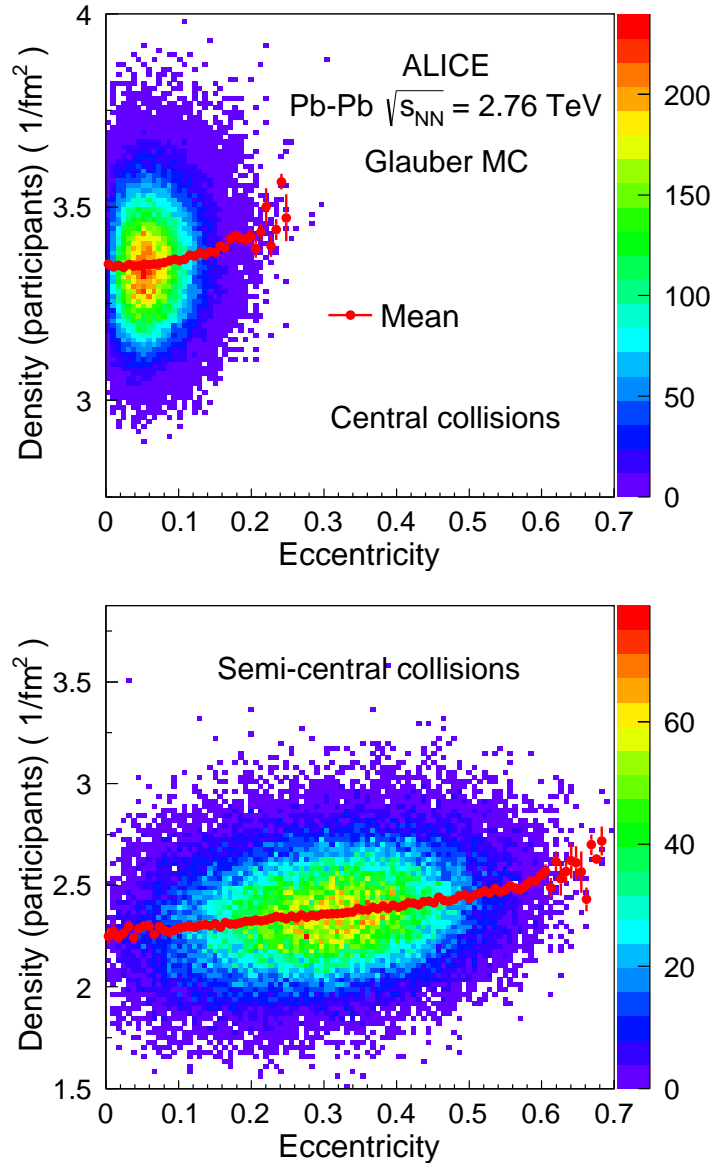


Fig. 13: Participant density as a function of the participant eccentricity estimated in a Glauber Monte Carlo model for central (top) and semi-central (bottom) collisions.

Two narrow centrality classes, selected based on the simulated charged particle multiplicity, roughly corresponding to 0-2% (central) and 30-32% (semi-central), are studied in Fig. 13. The observed correlation between the density and the participant eccentricity is reminiscent of the correlation between radial flow and event shape measured in this paper. The average density in events with the 10% largest ε is about 1% (7%) larger than in events with the smallest ε for central (semi-central) collisions, qualitatively consistent with what is observed in Fig. 10 and Fig. 11, where the effect of the ESE selection is much stronger for semi-central collisions. This reinforces our conclusion that ESE is an effective tool to select the initial shape and density, thereby opening the possibility of further studies.

A quantitative comparison would require a full hydrodynamical calculation. The correlation can in fact be modified by the transport in the hydrodynamic phase. In particular, it was shown [7, 44] that in a system with a finite shear viscosity the flow coefficients, obtained for a given set of initial eccentricities, are reduced as compared to the ideal hydrodynamics case. At the same time, shear viscosity increases the radial flow. In principle, bulk viscosity reduces the radial flow, reducing the correlation observed

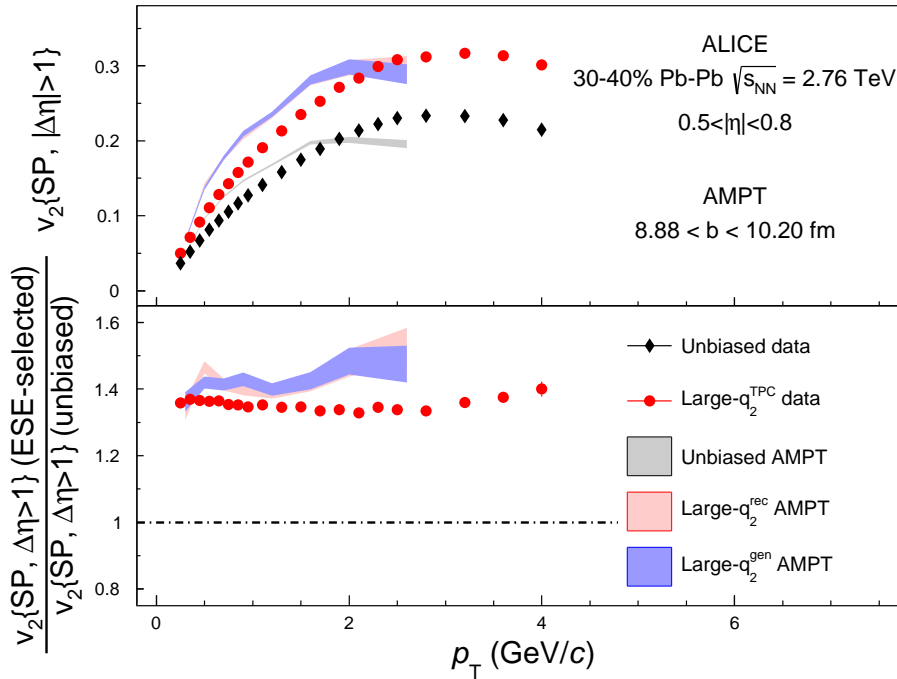


Fig. 14: Measurement of $v_2\{\text{SP}\}$ as a function of p_T , for the unbiased sample and for the large- q_2 sample (top panel) and ratio between the large- q_2 result over the unbiased result (bottom panel). Data points (full markers) are compared with AMPT Monte Carlo model (bands). Only statistical uncertainties are plotted (systematic uncertainties are smaller than the markers).

in this paper, but the latter effect was estimated to be negligible [44]. Therefore, the measurement we present in this paper is sensitive to the interplay of initial conditions and transport coefficients in the hydrodynamic phase. As such, it poses stringent constraints on hydrodynamic calculations, and it could allow the extraction of the value of average shear viscosity at the LHC.

To further understand this effect, we studied it in AMPT, a model known to reproduce many of the flow observables measured at the LHC [33]. This model is based on HIJING [45] to describe the initial conditions and on the Zhang’s parton cascade [46] to describe the partonic evolution. The *string melting* configuration, described in [47], is used. To assess the impact of the detector resolution on the q_2 selection, the simulated AMPT events were transported through the ALICE apparatus using the GEANT [34] transport model. The q_2 was computed using either the reconstructed Monte Carlo tracks (q_2^{rec}) or the generated primary particles in the same kinematic range (q_2^{gen}). The elliptic flow and the transverse momentum distribution are calculated using generated Monte Carlo particles. Since the charged particle multiplicity distribution is different in AMPT and data, the q_2 selection is calibrated in the model as a function of multiplicity. The results are shown in Fig. 14 for the charged hadrons elliptic flow and in Fig. 15 for the transverse momentum distribution of charged hadrons. Using either q_2^{rec} or q_2^{gen} does not introduce any significant difference on the effect of the selection. This indicates that detector resolution effects are negligible for the q_2^{TPC} selection. The V0 detectors, on the other hand, have a coarser azimuthal resolution and are sensitive to fluctuations in the energy deposition of incident particles. However, the study with the relaxed TPC selection discussed in Sect. 4 demonstrates that the properties of the ESE selected events are mostly determined by the average $v_2\{\text{SP}\}$ value. It is therefore advised that in any comparison of this data to theoretical models the selection in the model is tuned as to reproduce the average change in $v_2\{\text{SP}\}$ at mid-rapidity.

The p_T dependence of the elliptic flow observed in data is not reproduced in AMPT (top panel). This

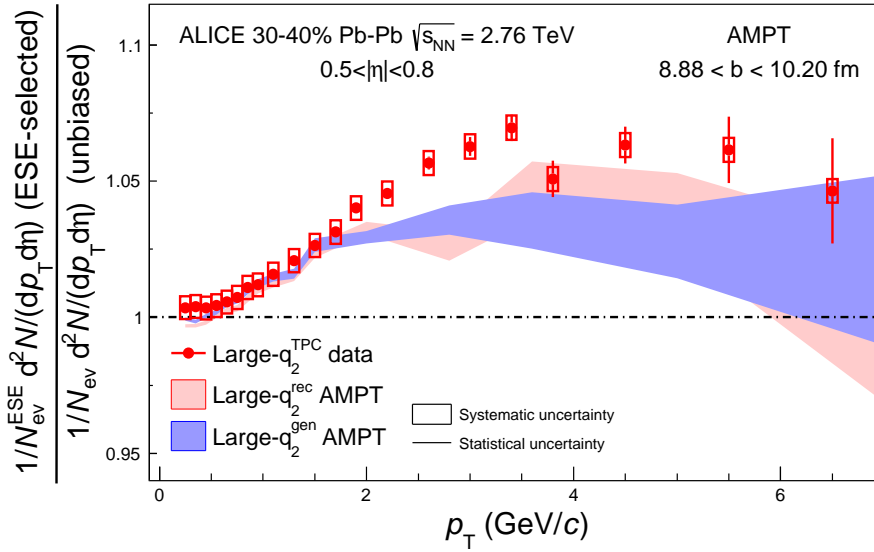


Fig. 15: Ratio of the p_T distribution of charged hadrons in the large- q_2 sample to the unbiased sample for the q_2^{TPC} selection. Data points (full markers) are compared with AMPT Monte Carlo model (bands).

model reproduces however the magnitude of the modification as well as the flatness of the ratio as a function of p_T .

The effect of the ESE selection on the p_T distribution of charged particles is well reproduced by AMPT below $p_T = 2$ GeV/ c , as shown in Fig. 15. However, the magnitude of the effect at intermediate p_T ($2 < p_T < 6$ GeV/ c) is underestimated in AMPT. As previously observed for the v_2 measurement, a good agreement is observed between the selection based on q_2^{gen} and q_2^{rec} .

6 Conclusions

In summary, the first application of the Event Shape Engineering (ESE) technique to Pb–Pb collisions data measured by ALICE at $\sqrt{s_{NN}} = 2.76$ TeV has been presented.

The elliptic flow at mid-rapidity is observed to increase as a function of the q_2 calculated in the central or forward rapidity regions. The modification of the v_2 coefficient as a function of p_T is nearly flat below $p_T = 4$ GeV/ c , suggesting that this technique allows the selection of a global property of the collision, likely related with the geometry of the participant nucleons in the initial state. In the region above $p_T > 5$ GeV/ c a small increase is observed within the large statistical uncertainties, possibly due to a small non-flow contamination. In this transverse momentum range the elliptic flow is believed to be driven by the different path-length traversed in- and out-of-plane by high- p_T partons in the deconfined medium, rather than by the hydrodynamic evolution of the system.

The p_T -distributions of unidentified hadrons in the p_T region ($0 < p_T < 5$ GeV/ c) are harder (softer) in event with large- q_2 (small- q_2) values.

Identified pions, kaons and protons show a similar behavior with a clear mass ordering in the ratio between the large- q_2 and the unbiased spectra, thus suggesting this effect to be due to a stronger radial flow in such events. Glauber Monte Carlo calculations reveal a correlation between the transverse participant density and the participant eccentricity which could be the origin of this effect. This indicates that at least part of the correlation is generated in the initial state. However, these measurements are also sensitive to the transport coefficients in the hydrodynamic evolution. A quantitative comparison would require a full hydrodynamic calculation and may provide stringent constraints both on shear and bulk viscosity.

Acknowledgments

The ALICE Collaboration would like to thank all its engineers and technicians for their invaluable contributions to the construction of the experiment and the CERN accelerator teams for the outstanding performance of the LHC complex. The ALICE Collaboration gratefully acknowledges the resources and support provided by all Grid centres and the Worldwide LHC Computing Grid (WLCG) collaboration. The ALICE Collaboration acknowledges the following funding agencies for their support in building and running the ALICE detector: State Committee of Science, World Federation of Scientists (WFS) and Swiss Fonds Kidagan, Armenia, Conselho Nacional de Desenvolvimento Científico e Tecnológico (CNPq), Financiadora de Estudos e Projetos (FINEP), Fundação de Amparo à Pesquisa do Estado de São Paulo (FAPESP); National Natural Science Foundation of China (NSFC), the Chinese Ministry of Education (CMOE) and the Ministry of Science and Technology of China (MSTC); Ministry of Education and Youth of the Czech Republic; Danish Natural Science Research Council, the Carlsberg Foundation and the Danish National Research Foundation; The European Research Council under the European Community's Seventh Framework Programme; Helsinki Institute of Physics and the Academy of Finland; French CNRS-IN2P3, the 'Region Pays de Loire', 'Region Alsace', 'Region Auvergne' and CEA, France; German Bundesministerium für Bildung, Wissenschaft, Forschung und Technologie (BMBF) and the Helmholtz Association; General Secretariat for Research and Technology, Ministry of Development, Greece; Hungarian Országos Tudományos Kutatási Alapprogramok (OTKA) and National Office for Research and Technology (NKTH); Department of Atomic Energy and Department of Science and Technology of the Government of India; Istituto Nazionale di Fisica Nucleare (INFN) and Centro Fermi - Museo Storico della Fisica e Centro Studi e Ricerche "Enrico Fermi", Italy; MEXT Grant-in-Aid for Specially Promoted Research, Japan; Joint Institute for Nuclear Research, Dubna; National Research Foundation of Korea (NRF); Consejo Nacional de Ciencia y Tecnología (CONACYT), Dirección General de Asuntos del Personal Académico (DGAPA), México, Amérique Latine Formation académique - European Commission (ALFA-EC) and the EPLANET Program (European Particle Physics Latin American Network); Stichting voor Fundamenteel Onderzoek der Materie (FOM) and the Nederlandse Organisatie voor Wetenschappelijk Onderzoek (NWO), Netherlands; Research Council of Norway (NFR); National Science Centre, Poland; Ministry of National Education/Institute for Atomic Physics and National Council of Scientific Research in Higher Education (CNCSI-UEFISCDI), Romania; Ministry of Education and Science of Russian Federation, Russian Academy of Sciences, Russian Federal Agency of Atomic Energy, Russian Federal Agency for Science and Innovations and The Russian Foundation for Basic Research; Ministry of Education of Slovakia; Department of Science and Technology, South Africa; Centro de Investigaciones Energéticas, Medioambientales y Tecnológicas (CIEMAT), E-Infrastructure shared between Europe and Latin America (EELA), Ministerio de Economía y Competitividad (MINECO) of Spain, Xunta de Galicia (Consellería de Educación), Centro de Aplicaciones Tecnológicas y Desarrollo Nuclear (CEADEN), Cubaenergía, Cuba, and IAEA (International Atomic Energy Agency); Swedish Research Council (VR) and Knut & Alice Wallenberg Foundation (KAW); Ukraine Ministry of Education and Science; United Kingdom Science and Technology Facilities Council (STFC); The United States Department of Energy, the United States National Science Foundation, the State of Texas, and the State of Ohio; Ministry of Science, Education and Sports of Croatia and Unity through Knowledge Fund, Croatia. Council of Scientific and Industrial Research (CSIR), New Delhi, India

References

- [1] **Wuppertal-Budapest** Collaboration, S. Borsanyi *et al.*, "Is there still any T_c mystery in lattice QCD? Results with physical masses in the continuum limit III," *JHEP* **1009** (2010) 073, arXiv:1005.3508 [hep-lat].
- [2] A. Bazavov, T. Bhattacharya, M. Cheng, C. DeTar, H. Ding, *et al.*, "The chiral and deconfinement aspects of the QCD transition," *Phys.Rev.* **D85** (2012) 054503, arXiv:1111.1710 [hep-lat].

- [3] N. Armesto, N. Borghini, S. Jeon, U. Wiedemann, S. Abreu, *et al.*, “Heavy Ion Collisions at the LHC - Last Call for Predictions,” *J.Phys.* **G35** (2008) 054001, arXiv:0711.0974 [hep-ph].
- [4] J. Schukraft, “Heavy Ion Physics at the LHC: What’s new ? What’s next ?,” arXiv:1311.1429 [hep-ex].
- [5] Y. Akiba, A. Angerami, H. Caines, A. Frawley, U. Heinz, *et al.*, “The Hot QCD White Paper: Exploring the Phases of QCD at RHIC and the LHC,” arXiv:1502.02730 [nucl-ex].
- [6] C. Gale, S. Jeon, and B. Schenke, “Hydrodynamic Modeling of Heavy-Ion Collisions,” *Int.J.Mod.Phys.* **A28** (2013) 1340011, arXiv:1301.5893 [nucl-th].
- [7] U. Heinz and R. Snellings, “Collective flow and viscosity in relativistic heavy-ion collisions,” *Ann.Rev.Nucl.Part.Sci.* **63** (2013) 123–151, arXiv:1301.2826 [nucl-th].
- [8] **ATLAS** Collaboration, G. Aad *et al.*, “Measurement of event-plane correlations in $\sqrt{s_{NN}} = 2.76$ TeV lead-lead collisions with the ATLAS detector,” *Phys.Rev.* **C90** no. 2, (2014) 024905, arXiv:1403.0489 [hep-ex].
- [9] **PHOBOS** Collaboration, B. Alver *et al.*, “System size, energy, pseudorapidity, and centrality dependence of elliptic flow,” *Phys.Rev.Lett.* **98** (2007) 242302, arXiv:nucl-ex/0610037 [nucl-ex].
- [10] **PHOBOS** Collaboration, B. Alver *et al.*, “Event-by-Event Fluctuations of Azimuthal Particle Anisotropy in Au + Au Collisions at $\sqrt{s_{NN}} = 200$ GeV,” *Phys.Rev.Lett.* **104** (2010) 142301, arXiv:nucl-ex/0702036 [nucl-ex].
- [11] **ATLAS** Collaboration, G. Aad *et al.*, “Measurement of the distributions of event-by-event flow harmonics in lead-lead collisions at $\sqrt{s_{NN}} = 2.76$ TeV with the ATLAS detector at the LHC,” *JHEP* **1311** (2013) 183, arXiv:1305.2942 [hep-ex].
- [12] **ALICE** Collaboration, B. Abelev *et al.*, “Anisotropic flow of charged hadrons, pions and (anti-)protons measured at high transverse momentum in Pb-Pb collisions at $\sqrt{s_{NN}} = 2.76$ TeV,” *Phys.Lett.* **B719** (2013) 18–28, arXiv:1205.5761 [nucl-ex].
- [13] **ALICE** Collaboration, K. Aamodt *et al.*, “Higher harmonic anisotropic flow measurements of charged particles in Pb-Pb collisions at $\sqrt{s_{NN}} = 2.76$ TeV,” *Phys.Rev.Lett.* **107** (2011) 032301, arXiv:1105.3865 [nucl-ex].
- [14] **CMS** Collaboration, S. Chatrchyan *et al.*, “Studies of azimuthal dihadron correlations in ultra-central PbPb collisions at $\sqrt{s_{NN}} = 2.76$ TeV,” *JHEP* **1402** (2014) 088, arXiv:1312.1845 [nucl-ex].
- [15] **ALICE** Collaboration, B. B. Abelev *et al.*, “Long-range angular correlations of π , K and p in p-Pb collisions at $\sqrt{s_{NN}} = 5.02$ TeV,” *Phys.Lett.* **B726** (2013) 164–177, arXiv:1307.3237 [nucl-ex].
- [16] **ALICE** Collaboration, B. B. Abelev *et al.*, “Multiplicity Dependence of Pion, Kaon, Proton and Lambda Production in p-Pb Collisions at $\sqrt{s_{NN}} = 5.02$ TeV,” *Phys.Lett.* **B728** (2014) 25–38, arXiv:1307.6796 [nucl-ex].
- [17] K. Werner, M. Bleicher, B. Guiot, I. Karpenko, and T. Pierog, “Evidence for flow in pPb collisions at 5 TeV from v_2 mass splitting,” *Phys.Rev.Lett.* **112** (2014) 232301, arXiv:1307.4379 [nucl-th].
- [18] E. Shuryak and I. Zahed, “High-multiplicity pp and pA collisions: Hydrodynamics at its edge,” *Phys.Rev.* **C88** no. 4, (2013) 044915, arXiv:1301.4470 [hep-ph].
- [19] P. Boek, W. Broniowski, and G. Torrieri, “Hydrodynamic models of particle production - p-Pb collisions,” *J.Phys.Conf.Ser.* **509** (2014) 012017, arXiv:1309.7782 [nucl-th].
- [20] J. Schukraft, A. Timmins, and S. A. Voloshin, “Ultra-relativistic nuclear collisions: event shape engineering,” *Phys.Lett.* **B719** (2013) 394–398, arXiv:1208.4563 [nucl-ex].
- [21] F. G. Gardim, F. Grassi, M. Luzum, and J.-Y. Ollitrault, “Characterizing the hydrodynamic

- response to the initial conditions,” *Nucl.Phys.* **A904-905** (2013) 503c–506c, arXiv:1210.8422 [nucl-th].
- [22] S. A. Voloshin, A. M. Poskanzer, and R. Snellings, “Collective phenomena in non-central nuclear collisions,” arXiv:0809.2949 [nucl-ex].
- [23] **ATLAS** Collaboration, G. Aad *et al.*, “Measurement of the correlation between flow harmonics of different order in lead-lead collisions at $\sqrt{s_{NN}}=2.76$ TeV with the ATLAS detector,” arXiv:1504.01289 [hep-ex].
- [24] **ALICE** Collaboration, K. Aamodt *et al.*, “The ALICE experiment at the CERN LHC,” *JINST* **3** (2008) S08002.
- [25] J. Alme, Y. Andres, H. Appelshauer, S. Bablok, N. Bialas, *et al.*, “The ALICE TPC, a large 3-dimensional tracking device with fast readout for ultra-high multiplicity events,” *Nucl.Instrum.Meth.* **A622** (2010) 316–367, arXiv:1001.1950 [physics.ins-det].
- [26] **ALICE** Collaboration, B. B. Abelev *et al.*, “Performance of the ALICE Experiment at the CERN LHC,” *Int.J.Mod.Phys.* **A29** (2014) 1430044, arXiv:1402.4476 [nucl-ex].
- [27] A. Collaboration, “Technical design report of the time projection chamber,” tech. rep., CERN/LHCC 2000-001, 2000.
- [28] **ALICE** Collaboration, E. Abbas *et al.*, “Performance of the ALICE VZERO system,” *JINST* **8** (2013) P10016, arXiv:1306.3130 [nucl-ex].
- [29] **ALICE** Collaboration, B. Abelev *et al.*, “Centrality determination of Pb-Pb collisions at $\sqrt{s_{NN}} = 2.76$ TeV with ALICE,” *Phys.Rev.* **C88** no. 4, (2013) 044909, arXiv:1301.4361 [nucl-ex].
- [30] **ALICE** Collaboration, K. Aamodt *et al.*, “Charged-particle multiplicity density at mid-rapidity in central Pb-Pb collisions at $\sqrt{s_{NN}} = 2.76$ TeV,” *Phys.Rev.Lett.* **105** (2010) 252301, arXiv:1011.3916 [nucl-ex].
- [31] **ALICE** Collaboration, K. Aamodt *et al.*, “Centrality dependence of the charged-particle multiplicity density at mid-rapidity in Pb-Pb collisions at $\sqrt{s_{NN}} = 2.76$ TeV,” *Phys.Rev.Lett.* **106** (2011) 032301, arXiv:1012.1657 [nucl-ex].
- [32] **STAR** Collaboration, C. Adler *et al.*, “Elliptic flow from two and four particle correlations in Au+Au collisions at $s(NN)^{1/2} = 130$ -GeV,” *Phys.Rev.* **C66** (2002) 034904, arXiv:nucl-ex/0206001 [nucl-ex].
- [33] Z.-W. Lin, C. M. Ko, B.-A. Li, B. Zhang, and S. Pal, “A Multi-phase transport model for relativistic heavy ion collisions,” *Phys.Rev.* **C72** (2005) 064901, arXiv:nucl-th/0411110 [nucl-th].
- [34] R. Brun, F. Carminati, and S. Giani, “GEANT Detector Description and Simulation Tool,” CERN-W5013.
- [35] **ALICE** Collaboration, B. Abelev *et al.*, “Measurement of charged jet suppression in Pb-Pb collisions at $\sqrt{s_{NN}} = 2.76$ TeV,” *JHEP* **03** (2014) 013, arXiv:1311.0633 [nucl-ex].
- [36] R. Barlow, “Systematic errors: Facts and fictions,” arXiv:hep-ex/0207026 [hep-ex].
- [37] **ALICE** Collaboration, B. Abelev *et al.*, “Centrality Dependence of Charged Particle Production at Large Transverse Momentum in Pb–Pb Collisions at $\sqrt{s_{NN}} = 2.76$ TeV,” *Phys.Lett.* **B720** (2013) 52–62, arXiv:1208.2711 [hep-ex].
- [38] **ALICE** Collaboration, B. Abelev *et al.*, “Centrality dependence of π , K, p production in Pb-Pb collisions at $\sqrt{s_{NN}} = 2.76$ TeV,” *Phys.Rev.* **C88** no. 4, (2013) 044910, arXiv:1303.0737 [hep-ex].
- [39] **ALICE** Collaboration, B. B. Abelev *et al.*, “Elliptic flow of identified hadrons in Pb-Pb collisions at $\sqrt{s_{NN}} = 2.76$ TeV,” arXiv:1405.4632 [nucl-ex].
- [40] E. Schnedermann, J. Sollfrank, and U. W. Heinz, “Thermal phenomenology of hadrons from 200-A/GeV S+S collisions,” *Phys.Rev.* **C48** (1993) 2462–2475,

- arXiv:nucl-th/9307020 [nucl-th].
- [41] S. Voloshin and A. M. Poskanzer, “The Physics of the centrality dependence of elliptic flow,” *Phys.Lett.* **B474** (2000) 27–32, arXiv:nucl-th/9906075 [nucl-th].
- [42] B. Alver, B. Back, M. Baker, M. Ballintijn, D. Barton, *et al.*, “Importance of correlations and fluctuations on the initial source eccentricity in high-energy nucleus-nucleus collisions,” *Phys.Rev.* **C77** (2008) 014906, arXiv:0711.3724 [nucl-ex].
- [43] S. A. Voloshin, A. M. Poskanzer, A. Tang, and G. Wang, “Elliptic flow in the Gaussian model of eccentricity fluctuations,” *Phys.Lett.* **B659** (2008) 537–541, arXiv:0708.0800 [nucl-th].
- [44] H. Song and U. W. Heinz, “Interplay of shear and bulk viscosity in generating flow in heavy-ion collisions,” *Phys.Rev.* **C81** (2010) 024905, arXiv:0909.1549 [nucl-th].
- [45] M. Gyulassy and X.-N. Wang, “HIJING 1.0: A Monte Carlo program for parton and particle production in high-energy hadronic and nuclear collisions,” *Comput.Phys.Commun.* **83** (1994) 307, arXiv:nucl-th/9502021 [nucl-th].
- [46] B. Zhang, “ZPC 1.0.1: A Parton cascade for ultrarelativistic heavy ion collisions,” *Comput.Phys.Commun.* **109** (1998) 193–206, arXiv:nucl-th/9709009 [nucl-th].
- [47] **ALICE** Collaboration, B. Abelev *et al.*, “Charge correlations using the balance function in Pb-Pb collisions at $\sqrt{s_{NN}} = 2.76$ TeV,” *Phys.Lett.* **B723** (2013) 267–279, arXiv:1301.3756 [nucl-ex].

A The ALICE Collaboration

J. Adam⁴⁰, D. Adamová⁸³, M.M. Aggarwal⁸⁷, G. Aglieri Rinella³⁶, M. Agnello¹¹¹, N. Agrawal⁴⁸, Z. Ahammed¹³², S.U. Ahn⁶⁸, I. Aimo^{94,111}, S. Aiola¹³⁶, M. Ajaz¹⁶, A. Akhmedov⁵⁸, S.N. Alam¹³², D. Aleksandrov¹⁰⁰, B. Alessandro¹¹¹, D. Alexandre¹⁰², R. Alfaro Molina⁶⁴, A. Alici^{105,12}, A. Alkin³, J.R.M. Almaraz¹¹⁹, J. Alme³⁸, T. Alt⁴³, S. Altinpinar¹⁸, I. Altsybeev¹³¹, C. Alves Garcia Prado¹²⁰, C. Andrei⁷⁸, A. Andronic⁹⁷, V. Anguelov⁹³, J. Anielski⁵⁴, T. Antičić⁹⁸, F. Antinori¹⁰⁸, P. Antonioli¹⁰⁵, L. Aphecetche¹¹³, H. Appelshäuser⁵³, S. Arcelli²⁸, N. Armesto¹⁷, R. Arnaldi¹¹¹, I.C. Arsene²², M. Arslandok⁵³, B. Audurier¹¹³, A. Augustinus³⁶, R. Averbeck⁹⁷, M.D. Azmi¹⁹, M. Bach⁴³, A. Badalà¹⁰⁷, Y.W. Baek⁴⁴, S. Bagnasco¹¹¹, R. Bailhache⁵³, R. Bala⁹⁰, A. Baldisseri¹⁵, F. Baltasar Dos Santos Pedrosa³⁶, R.C. Baral⁶¹, A.M. Barbano¹¹¹, R. Barbera²⁹, F. Barile³³, G.G. Barnaföldi¹³⁵, L.S. Barnby¹⁰², V. Barret⁷⁰, P. Bartalini⁷, K. Barth³⁶, J. Bartke¹¹⁷, E. Bartsch⁵³, M. Basile²⁸, N. Bastid⁷⁰, S. Basu¹³², B. Bathen⁵⁴, G. Batigne¹¹³, A. Batista Camejo⁷⁰, B. Batyunya⁶⁶, P.C. Batzing²², I.G. Bearden⁸⁰, H. Beck⁵³, C. Bedda¹¹¹, N.K. Behera^{48,49}, I. Belikov⁵⁵, F. Bellini²⁸, H. Bello Martinez², R. Bellwied¹²², R. Belmont¹³⁴, E. Belmont-Moreno⁶⁴, V. Belyaev⁷⁶, G. Bencedi¹³⁵, S. Beole²⁷, I. Berceanu⁷⁸, A. Bercuci⁷⁸, Y. Berdnikov⁸⁵, D. Berenyi¹³⁵, R.A. Bertens⁵⁷, D. Berzano^{36,27}, L. Betev³⁶, A. Bhasin⁹⁰, I.R. Bhat⁹⁰, A.K. Bhati⁸⁷, B. Bhattacharjee⁴⁵, J. Bhom¹²⁸, L. Bianchi¹²², N. Bianchi⁷², C. Bianchin^{134,57}, J. Bielčik⁴⁰, J. Bielčíková⁸³, A. Bilandzic⁸⁰, R. Biswas⁴, S. Biswas⁷⁹, S. Bjelogrić⁵⁷, J.T. Blair¹¹⁸, F. Blanco¹⁰, D. Blau¹⁰⁰, C. Blume⁵³, F. Bock^{93,74}, A. Bogdanov⁷⁶, H. Bøggild⁸⁰, L. Boldizsár¹³⁵, M. Bombara⁴¹, J. Book⁵³, H. Borel¹⁵, A. Borissov⁹⁶, M. Borri⁸², F. Bossu⁶⁵, E. Botta²⁷, S. Böttger⁵², P. Braun-Munzinger⁹⁷, M. Bregant¹²⁰, T. Breitner⁵², T.A. Broker⁵³, T.A. Browning⁹⁵, M. Broz⁴⁰, E.J. Brucken⁴⁶, E. Bruna¹¹¹, G.E. Bruno³³, D. Budnikov⁹⁹, H. Buesching⁵³, S. Bufalino^{27,111}, P. Buncic³⁶, O. Busch^{128,93}, Z. Buthelezi⁶⁵, J.B. Butt¹⁶, J.T. Buxton²⁰, D. Caffarri³⁶, X. Cai⁷, H. Caines¹³⁶, L. Calero Diaz⁷², A. Caliva⁵⁷, E. Calvo Villar¹⁰³, P. Camerini²⁶, F. Carena³⁶, W. Carena³⁶, F. Carnesecchi²⁸, J. Castillo Castellanos¹⁵, A.J. Castro¹²⁵, E.A.R. Casula²⁵, C. Cavicchioli³⁶, C. Ceballos Sanchez⁹, J. Cepila⁴⁰, P. Cerello¹¹¹, J. Cercala¹¹⁵, B. Chang¹²³, S. Chapeland³⁶, M. Chartier¹²⁴, J.L. Charvet¹⁵, S. Chattopadhyay¹³², S. Chattopadhyay¹⁰¹, V. Chelnokov³, M. Cherney⁸⁶, C. Cheshkov¹³⁰, B. Cheynis¹³⁰, V. Chibante Barroso³⁶, D.D. Chinellato¹²¹, P. Chochula³⁶, K. Choi⁹⁶, M. Chojnacki⁸⁰, S. Choudhury¹³², P. Christakoglou⁸¹, C.H. Christensen⁸⁰, P. Christiansen³⁴, T. Chujo¹²⁸, S.U. Chung⁹⁶, Z. Chuhui⁵⁷, C. Cicalo¹⁰⁶, L. Cifarelli^{12,28}, F. Cindolo¹⁰⁵, J. Cleymans⁸⁹, F. Colamaria³³, D. Colella^{36,33,59}, A. Collu²⁵, M. Colocci²⁸, G. Conesa Balbastre⁷¹, Z. Conesa del Valle⁵¹, M.E. Connors¹³⁶, J.G. Contreras^{11,40}, T.M. Cormier⁸⁴, Y. Corrales Morales²⁷, I. Cortés Maldonado², P. Cortese³², M.R. Cosentino¹²⁰, F. Costa³⁶, P. Crochet⁷⁰, R. Cruz Albino¹¹, E. Cuautle⁶³, L. Cunqueiro³⁶, T. Dahms^{92,37}, A. Dainese¹⁰⁸, A. Danu⁶², D. Das¹⁰¹, I. Das^{101,51}, S. Das⁴, A. Dash¹²¹, S. Dash⁴⁸, S. De¹²⁰, A. De Caro^{31,12}, G. de Cataldo¹⁰⁴, J. de Cuveland⁴³, A. De Falco²⁵, D. De Gruttola^{12,31}, N. De Marco¹¹¹, S. De Pasquale³¹, A. Deisting^{97,93}, A. Deloff⁷⁷, E. Dénes^{135,i}, G. D'Erasmus³³, D. Di Bari³³, A. Di Mauro³⁶, P. Di Nezza⁷², M.A. Diaz Corchero¹⁰, T. Dietel⁸⁹, P. Dillenseger⁵³, R. Divià³⁶, Ø. Djuvsland¹⁸, A. Dobrin^{57,81}, T. Dobrowolski^{77,i}, D. Domenicis Gimenez¹²⁰, B. Dönigus⁵³, O. Dordic²², T. Drozhzhova⁵³, A.K. Dubey¹³², A. Dubla⁵⁷, L. Ducroux¹³⁰, P. Dupieux⁷⁰, R.J. Ehlers¹³⁶, D. Elia¹⁰⁴, H. Engel⁵², B. Erasmus^{36,113}, I. Erdemir⁵³, F. Erhardt¹²⁹, D. Eschweiler⁴³, B. Espagnon⁵¹, M. Estienne¹¹³, S. Esumi¹²⁸, J. Eum⁹⁶, D. Evans¹⁰², S. Evdokimov¹¹², G. Eyyubova⁴⁰, L. Fabbietti^{37,92}, D. Fabris¹⁰⁸, J. Faivre⁷¹, A. Fantoni⁷², M. Fasel⁷⁴, L. Feldkamp⁵⁴, D. Felea⁶², A. Feliciello¹¹¹, G. Feofilov¹³¹, J. Ferencei⁸³, A. Fernández Téllez², E.G. Ferreira¹⁷, A. Ferretti²⁷, A. Festanti³⁰, V.J.G. Feuillard^{15,70}, J. Figiel¹¹⁷, M.A.S. Figueroa^{124,120}, S. Filchagin⁹⁹, D. Finogeev⁵⁶, F.M. Fionda²⁵, E.M. Fiore³³, M.G. Fleck⁹³, M. Floris³⁶, S. Foertsch⁶⁵, P. Foka⁹⁷, S. Fokin¹⁰⁰, E. Fragiaco¹¹⁰, A. Francescon^{36,30}, U. Frankenfeld⁹⁷, U. Fuchs³⁶, C. Furget⁷¹, A. Furs⁵⁶, M. Fusco Girard³¹, J.J. Gaardhøje⁸⁰, M. Gagliardi²⁷, A.M. Gago¹⁰³, M. Gallio²⁷, D.R. Gangadharan⁷⁴, P. Ganoti⁸⁸, C. Gao⁷, C. Garabatos⁹⁷, E. Garcia-Solis¹³, C. Gargiulo³⁶, P. Gasik^{92,37}, M. Germain¹¹³, A. Gheata³⁶, M. Gheata^{62,36}, P. Ghosh¹³², S.K. Ghosh⁴, P. Gianotti⁷², P. Giubellino³⁶, P. Giubilato³⁰, E. Gladysz-Dziadus¹¹⁷, P. Glässel⁹³, D.M. Gómez Coral⁶⁴, A. Gomez Ramirez⁵², P. González-Zamora¹⁰, S. Gorunov⁴³, L. Görlich¹¹⁷, S. Gotovac¹¹⁶, V. Grabski⁶⁴, L.K. Graczykowski¹³³, K.L. Graham¹⁰², A. Grelli⁵⁷, A. Grigoras³⁶, C. Grigoras³⁶, V. Grigoriev⁷⁶, A. Grigoryan¹, S. Grigoryan⁶⁶, B. Grinyov³, N. Grion¹¹⁰, J.F. Grosse-Oetringhaus³⁶, J.-Y. Grossiord¹³⁰, R. Grosso³⁶, F. Guber⁵⁶, R. Guernane⁷¹, B. Guerzoni²⁸, K. Gulbrandsen⁸⁰, H. Gulkanyan¹, T. Gunji¹²⁷, A. Gupta⁹⁰, R. Gupta⁹⁰, R. Haake⁵⁴, Ø. Haaland¹⁸, C. Hadjidakis⁵¹, M. Haiduc⁶², H. Hamagaki¹²⁷, G. Hamar¹³⁵, A. Hansen⁸⁰, J.W. Harris¹³⁶, H. Hartmann⁴³, A. Harton¹³, D. Hatzifotiadou¹⁰⁵, S. Hayashi¹²⁷, S.T. Heckel⁵³, M. Heide⁵⁴, H. Helstrup³⁸, A. Herghelegiu⁷⁸, G. Herrera Corral¹¹, B.A. Hess³⁵, K.F. Hetland³⁸, T.E. Hilden⁴⁶, H. Hillemanns³⁶, B. Hippolyte⁵⁵, R. Hosokawa¹²⁸, P. Hristov³⁶, M. Huang¹⁸, T.J. Humanic²⁰, N. Hussain⁴⁵, T. Hussain¹⁹, D. Hutter⁴³, D.S. Hwang²¹, R. Ilkaev⁹⁹, I. Ilkiv⁷⁷, M. Inaba¹²⁸,

M. Ippolitov^{76,100}, M. Irfan¹⁹, M. Ivanov⁹⁷, V. Ivanov⁸⁵, V. Izucheev¹¹², P.M. Jacobs⁷⁴, S. Jadlovská¹¹⁵, C. Jahnke¹²⁰, H.J. Jang⁶⁸, M.A. Janik¹³³, P.H.S.Y. Jayarathna¹²², C. Jena³⁰, S. Jena¹²², R.T. Jimenez Bustamante⁹⁷, P.G. Jones¹⁰², H. Jung⁴⁴, A. Jusko¹⁰², P. Kalinak⁵⁹, A. Kalweit³⁶, J. Kamin⁵³, J.H. Kang¹³⁷, V. Kaplin⁷⁶, S. Kar¹³², A. Karasu Uysal⁶⁹, O. Karavichev⁵⁶, T. Karavicheva⁵⁶, L. Karayan^{93,97}, E. Karpechev⁵⁶, U. Kebschull⁵², R. Keidel¹³⁸, D.L.D. Keijdener⁵⁷, M. Keil³⁶, K.H. Khan¹⁶, M. Mohisin Khan¹⁹, P. Khan¹⁰¹, S.A. Khan¹³², A. Khanzadeev⁸⁵, Y. Kharlov¹¹², B. Kileng³⁸, B. Kim¹³⁷, D.W. Kim^{44,68}, D.J. Kim¹²³, H. Kim¹³⁷, J.S. Kim⁴⁴, M. Kim⁴⁴, M. Kim¹³⁷, S. Kim²¹, T. Kim¹³⁷, S. Kirsch⁴³, I. Kisel⁴³, S. Kiselev⁵⁸, A. Kisiel¹³³, G. Kiss¹³⁵, J.L. Klay⁶, C. Klein⁵³, J. Klein^{36,93}, C. Klein-Bösing⁵⁴, A. Kluge³⁶, M.L. Knichel⁹³, A.G. Knospe¹¹⁸, T. Kobayashi¹²⁸, C. Kobdaj¹¹⁴, M. Kofarago³⁶, T. Kollegger^{97,43}, A. Kolojvari¹³¹, V. Kondratiev¹³¹, N. Kondratyeva⁷⁶, E. Kondratyuk¹¹², A. Konevskikh⁵⁶, M. Kopcik¹¹⁵, M. Kour⁹⁰, C. Kouzinopoulos³⁶, O. Kovalenko⁷⁷, V. Kovalenko¹³¹, M. Kowalski¹¹⁷, G. Koyithatta Meethalevedu⁴⁸, J. Kral¹²³, I. Králik⁵⁹, A. Kravčáková⁴¹, M. Kretz⁴³, M. Krivda^{59,102}, F. Krizek⁸³, E. Kryshen³⁶, M. Krzewicki⁴³, A.M. Kubera²⁰, V. Kučera⁸³, T. Kugathasan³⁶, C. Kuhn⁵⁵, P.G. Kuijer⁸¹, A. Kumar⁹⁰, J. Kumar⁴⁸, L. Kumar^{79,87}, P. Kurashvili⁷⁷, A. Kurepin⁵⁶, A.B. Kurepin⁵⁶, A. Kuryakin⁹⁹, S. Kushpil⁸³, M.J. Kweon⁵⁰, Y. Kwon¹³⁷, S.L. La Pointe¹¹¹, P. La Rocca²⁹, C. Lagana Fernandes¹²⁰, I. Lakomov³⁶, R. Langoy⁴², C. Lara⁵², A. Lardeux¹⁵, A. Lattuca²⁷, E. Laudi³⁶, R. Lea²⁶, L. Leardini⁹³, G.R. Lee¹⁰², S. Lee¹³⁷, I. Legrand³⁶, F. Lehas⁸¹, R.C. Lemmon⁸², V. Lenti¹⁰⁴, E. Leogrande⁵⁷, I. León Monzón¹¹⁹, M. Leoncino²⁷, P. Lévai¹³⁵, S. Li^{7,70}, X. Li¹⁴, J. Lien⁴², R. Lietava¹⁰², S. Lindal²², V. Lindenstruth⁴³, C. Lippmann⁹⁷, M.A. Lisa²⁰, H.M. Ljunggren³⁴, D.F. Lodato⁵⁷, P.I. Loenne¹⁸, V. Loginov⁷⁶, C. Loizides⁷⁴, X. Lopez⁷⁰, E. López Torres⁹, A. Lowe¹³⁵, P. Luettig⁵³, M. Lunardon³⁰, G. Luparello²⁶, P.H.F.N.D. Luz¹²⁰, A. Maevskaya⁵⁶, M. Mager³⁶, S. Mahajan⁹⁰, S.M. Mahmood²², A. Maire⁵⁵, R.D. Majka¹³⁶, M. Malaev⁸⁵, I. Maldonado Cervantes⁶³, L. Malinina^{ii,66}, D. Mal'Kevich⁵⁸, P. Malzacher⁹⁷, A. Mamonov⁹⁹, V. Manko¹⁰⁰, F. Manso⁷⁰, V. Manzari^{36,104}, M. Marchisone²⁷, J. Mareš⁶⁰, G.V. Margagliotti²⁶, A. Margotti¹⁰⁵, J. Margutti⁵⁷, A. Marín⁹⁷, C. Markert¹¹⁸, M. Marquard⁵³, N.A. Martin⁹⁷, J. Martin Blanco¹¹³, P. Martinengo³⁶, M.I. Martínez², G. Martínez García¹¹³, M. Martinez Pedreira³⁶, Y. Martynov³, A. Mas¹²⁰, S. Masciocchi⁹⁷, M. Masera²⁷, A. Masoni¹⁰⁶, L. Massacrier¹¹³, A. Mastroserio³³, H. Masui¹²⁸, A. Matyja¹¹⁷, C. Mayer¹¹⁷, J. Mazer¹²⁵, M.A. Mazzoni¹⁰⁹, D. McDonald¹²², F. Meddi²⁴, Y. Melikyan⁷⁶, A. Menchaca-Rocha⁶⁴, E. Meninno³¹, J. Mercado Pérez⁹³, M. Meres³⁹, Y. Miake¹²⁸, M.M. Mieskolainen⁴⁶, K. Mikhaylov^{66,58}, L. Milano³⁶, J. Milosevic²², L.M. Minervini^{104,23}, A. Mischke⁵⁷, A.N. Mishra⁴⁹, D. Miśkowiec⁹⁷, J. Mitra¹³², C.M. Mitu⁶², N. Mohammadi⁵⁷, B. Mohanty^{132,79}, L. Molnar⁵⁵, L. Montaño Zetina¹¹, E. Montes¹⁰, M. Morando³⁰, D.A. Moreira De Godoy^{113,54}, S. Moretto³⁰, A. Morreale¹¹³, A. Morsch³⁶, V. Muccifora⁷², E. Mudnic¹¹⁶, D. Mühlheim⁵⁴, S. Muhuri¹³², M. Mukherjee¹³², J.D. Mulligan¹³⁶, M.G. Munhoz¹²⁰, S. Murray⁶⁵, L. Musa³⁶, J. Musinsky⁵⁹, B.K. Nandi⁴⁸, R. Nania¹⁰⁵, E. Nappi¹⁰⁴, M.U. Naru¹⁶, C. Nattrass¹²⁵, K. Nayak⁷⁹, T.K. Nayak¹³², S. Nazarenko⁹⁹, A. Nedosekin⁵⁸, L. Nellen⁶³, F. Ng¹²², M. Nicassio⁹⁷, M. Niculescu^{62,36}, J. Niedziela³⁶, B.S. Nielsen⁸⁰, S. Nikolaev¹⁰⁰, S. Nikulin¹⁰⁰, V. Nikulin⁸⁵, F. Noferini^{105,12}, P. Nomokonov⁶⁶, G. Nooren⁵⁷, J.C.C. Noris², J. Norman¹²⁴, A. Nyman¹⁰⁰, J. Nystrand¹⁸, H. Oeschler⁹³, S. Oh¹³⁶, S.K. Oh⁶⁷, A. Ohlson³⁶, A. Okatan⁶⁹, T. Okubo⁴⁷, L. Olah¹³⁵, J. Oleniacz¹³³, A.C. Oliveira Da Silva¹²⁰, M.H. Oliver¹³⁶, J. Onderwaater⁹⁷, C. Oppedisano¹¹¹, R. Orava⁴⁶, A. Ortiz Velasquez⁶³, A. Oskarsson³⁴, J. Otwinowski¹¹⁷, K. Oyama⁹³, M. Ozdemir⁵³, Y. Pachmayer⁹³, P. Pagano³¹, G. Paic⁶³, C. Pajares¹⁷, S.K. Pal¹³², J. Pan¹³⁴, A.K. Pandey⁴⁸, D. Pant⁴⁸, P. Papcun¹¹⁵, V. Papikyan¹, G.S. Pappalardo¹⁰⁷, P. Pareek⁴⁹, W.J. Park⁹⁷, S. Parmar⁸⁷, A. Passfeld⁵⁴, V. Paticchio¹⁰⁴, R.N. Patra¹³², B. Paul¹⁰¹, T. Peitzmann⁵⁷, H. Pereira Da Costa¹⁵, E. Pereira De Oliveira Filho¹²⁰, D. Peresunko^{100,76}, C.E. Pérez Lara⁸¹, E. Perez Lezama⁵³, V. Peskov⁵³, Y. Pestov⁵, V. Petráček⁴⁰, V. Petrov¹¹², M. Petrovici⁷⁸, C. Petta²⁹, S. Piano¹¹⁰, M. Pikna³⁹, P. Pillot¹¹³, O. Pinazza^{105,36}, L. Pinsky¹²², D.B. Piyarathna¹²², M. Płoskoń⁷⁴, M. Planinic¹²⁹, J. Pluta¹³³, S. Pochybova¹³⁵, P.L.M. Podesta-Lerma¹¹⁹, M.G. Poghosyan^{86,84}, B. Polichtchouk¹¹², N. Poljak¹²⁹, W. Poonsawat¹¹⁴, A. Pop⁷⁸, S. Porteboeuf-Houssais⁷⁰, J. Porter⁷⁴, J. Pospisil⁸³, S.K. Prasad⁴, R. Preghenella^{36,105}, F. Prino¹¹¹, C.A. Pruneau¹³⁴, I. Pshenichnov⁵⁶, M. Puccio¹¹¹, G. Puddu²⁵, P. Pujahari¹³⁴, V. Punin⁹⁹, J. Putschke¹³⁴, H. Qvigstad²², A. Rachevski¹¹⁰, S. Raha⁴, S. Rajput⁹⁰, J. Rak¹²³, A. Rakotozafindrabe¹⁵, L. Ramello³², F. Rami⁵⁵, R. Raniwala⁹¹, S. Raniwala⁹¹, S.S. Räsänen⁴⁶, B.T. Rangan⁵³, D. Rathee⁸⁷, K.F. Read¹²⁵, J.S. Real⁷¹, K. Redlich⁷⁷, R.J. Reed¹³⁴, A. Rehman¹⁸, P. Reichelt⁵³, F. Reidt^{93,36}, X. Ren⁷, R. Renfordt⁵³, A.R. Reolon⁷², A. Reshetin⁵⁶, F. Rettig⁴³, J.-P. Revol¹², K. Reygers⁹³, V. Riabov⁸⁵, R.A. Ricci⁷³, T. Richert³⁴, M. Richter²², P. Riedler³⁶, W. Riegler³⁶, F. Riggi²⁹, C. Ristea⁶², A. Rivetti¹¹¹, E. Rocco⁵⁷, M. Rodríguez Cahuantzi², A. Rodríguez Manso⁸¹, K. Røed²², E. Rogochaya⁶⁶, D. Rohr⁴³, D. Röhrich¹⁸, R. Romita¹²⁴, F. Ronchetti⁷², L. Ronflette¹¹³, P. Rosnet⁷⁰, A. Rossi^{30,36}, F. Roukoutakis⁸⁸, A. Roy⁴⁹, C. Roy⁵⁵, P. Roy¹⁰¹, A.J. Rubio Montero¹⁰, R. Rui²⁶, R. Russo²⁷, E. Ryabinkin¹⁰⁰, Y. Ryabov⁸⁵, A. Rybicki¹¹⁷, S. Sadovsky¹¹²,

K. Šafařík³⁶, B. Sahlmuller⁵³, P. Sahoo⁴⁹, R. Sahoo⁴⁹, S. Sahoo⁶¹, P.K. Sahu⁶¹, J. Saini¹³², S. Sakai⁷², M.A. Saleh¹³⁴, C.A. Salgado¹⁷, J. Salzwedel²⁰, S. Sambyal⁹⁰, V. Samsonov⁸⁵, X. Sanchez Castro⁵⁵, L. Sándor⁵⁹, A. Sandoval⁶⁴, M. Sano¹²⁸, D. Sarkar¹³², E. Scapparone¹⁰⁵, F. Scarlassara³⁰, R.P. Scharenberg⁹⁵, C. Schiaua⁷⁸, R. Schicker⁹³, C. Schmidt⁹⁷, H.R. Schmidt³⁵, S. Schuchmann⁵³, J. Schukraft³⁶, M. Schulc⁴⁰, T. Schuster¹³⁶, Y. Schutz^{113,36}, K. Schwarz⁹⁷, K. Schweda⁹⁷, G. Scioli²⁸, E. Scomparin¹¹¹, R. Scott¹²⁵, J.E. Seger⁸⁶, Y. Sekiguchi¹²⁷, D. Sekihata⁴⁷, I. Selyuzhenkov⁹⁷, K. Senosi⁶⁵, J. Seo^{96,67}, E. Serradilla^{64,10}, A. Sevcenco⁶², A. Shabanov⁵⁶, A. Shabetai¹¹³, O. Shadura³, R. Shahoyan³⁶, A. Shangaraev¹¹², A. Sharma⁹⁰, M. Sharma⁹⁰, M. Sharma⁹⁰, N. Sharma^{125,61}, K. Shigaki⁴⁷, K. Shtejer^{9,27}, Y. Sibiriyak¹⁰⁰, S. Siddhanta¹⁰⁶, K.M. Sielewicz³⁶, T. Siemiarczuk⁷⁷, D. Silvermyr^{84,34}, C. Silvestre⁷¹, G. Simatovic¹²⁹, G. Simonetti³⁶, R. Singaraju¹³², R. Singh⁷⁹, S. Singha^{132,79}, V. Singhal¹³², B.C. Sinha¹³², T. Sinha¹⁰¹, B. Sitar³⁹, M. Sitta³², T.B. Skaali²², M. Slupecki¹²³, N. Smirnov¹³⁶, R.J.M. Snellings⁵⁷, T.W. Snellman¹²³, C. Sogaard³⁴, R. Soltz⁷⁵, J. Song⁹⁶, M. Song¹³⁷, Z. Song⁷, F. Soramel³⁰, S. Sorensen¹²⁵, M. Spacek⁴⁰, E. Spiriti⁷², I. Sputowska¹¹⁷, M. Spyropoulou-Stassinaki⁸⁸, B.K. Srivastava⁹⁵, J. Stachel⁹³, I. Stan⁶², G. Stefanek⁷⁷, M. Steinpreis²⁰, E. Stenlund³⁴, G. Steyn⁶⁵, J.H. Stiller⁹³, D. Stocco¹¹³, P. Strmen³⁹, A.A.P. Suaide¹²⁰, T. Sugitate⁴⁷, C. Suire⁵¹, M. Suleymanov¹⁶, R. Sultanov⁵⁸, M. Šumbera⁸³, T.J.M. Symons⁷⁴, A. Szabo³⁹, A. Szanto de Toledo^{120,i}, I. Szarka³⁹, A. Szczepankiewicz³⁶, M. Szymanski¹³³, U. Tabassam¹⁶, J. Takahashi¹²¹, G.J. Tambave¹⁸, N. Tanaka¹²⁸, M.A. Tangaro³³, J.D. Tapia Takaki^{iii,51}, A. Tarantola Peloni⁵³, M. Tarhini⁵¹, M. Tariq¹⁹, M.G. Tarzila⁷⁸, A. Tauro³⁶, G. Tejada Muñoz², A. Telesca³⁶, K. Terasaki¹²⁷, C. Terrevoli^{30,25}, B. Teyssier¹³⁰, J. Thäder^{74,97}, D. Thomas¹¹⁸, R. Tieulent¹³⁰, A.R. Timmins¹²², A. Toia⁵³, S. Trogolo¹¹¹, V. Trubnikov³, W.H. Trzaska¹²³, T. Tsuji¹²⁷, A. Tumkin⁹⁹, R. Turrisi¹⁰⁸, T.S. Tveter²², K. Ullaland¹⁸, A. Uras¹³⁰, G.L. Usai²⁵, A. Utrobicic¹²⁹, M. Vajzer⁸³, M. Vala⁵⁹, L. Valencia Palomo⁷⁰, S. Vallero²⁷, J. Van Der Maarel⁵⁷, J.W. Van Hoorne³⁶, M. van Leeuwen⁵⁷, T. Vanat⁸³, P. Vande Vyvre³⁶, D. Varga¹³⁵, A. Vargas², M. Vargyas¹²³, R. Varma⁴⁸, M. Vasileiou⁸⁸, A. Vasiliev¹⁰⁰, A. Vauthier⁷¹, V. Vechernin¹³¹, A.M. Veen⁵⁷, M. Veldhoen⁵⁷, A. Velure¹⁸, M. Venaruzzo⁷³, E. Vercellin²⁷, S. Vergara Limón², R. Vernet⁸, M. Verweij^{134,36}, L. Vickovic¹¹⁶, G. Viesti^{30,i}, J. Viinikainen¹²³, Z. Vilakazi¹²⁶, O. Villalobos Baillie¹⁰², A. Vinogradov¹⁰⁰, L. Vinogradov¹³¹, Y. Vinogradov^{99,i}, T. Virgili³¹, V. Vislavicius³⁴, Y.P. Viyogi¹³², A. Vodopyanov⁶⁶, M.A. Völkl⁹³, K. Voloshin⁵⁸, S.A. Voloshin¹³⁴, G. Volpe^{135,36}, B. von Haller³⁶, I. Vorobyev^{37,92}, D. Vranic^{36,97}, J. Vrláková⁴¹, B. Vulpescu⁷⁰, A. Vyushin⁹⁹, B. Wagner¹⁸, J. Wagner⁹⁷, H. Wang⁵⁷, M. Wang^{7,113}, Y. Wang⁹³, D. Watanabe¹²⁸, Y. Watanabe¹²⁷, M. Weber³⁶, S.G. Weber⁹⁷, J.P. Wessels⁵⁴, U. Westerhoff⁵⁴, J. Wiechula³⁵, J. Wikne²², M. Wilde⁵⁴, G. Wilk⁷⁷, J. Wilkinson⁹³, M.C.S. Williams¹⁰⁵, B. Windelband⁹³, M. Winn⁹³, C.G. Yaldo¹³⁴, H. Yang⁵⁷, P. Yang⁷, S. Yano⁴⁷, Z. Yin⁷, H. Yokoyama¹²⁸, I.-K. Yoo⁹⁶, V. Yurchenko³, I. Yushmanov¹⁰⁰, A. Zaborowska¹³³, V. Zaccaro⁸⁰, A. Zaman¹⁶, C. Zampolli¹⁰⁵, H.J.C. Zanoli¹²⁰, S. Zaporozhets⁶⁶, N. Zardoshti¹⁰², A. Zarochentsev¹³¹, P. Závada⁶⁰, N. Zaviyalov⁹⁹, H. Zbroszczyk¹³³, I.S. Zgura⁶², M. Zhalov⁸⁵, H. Zhang^{18,7}, X. Zhang⁷⁴, Y. Zhang⁷, C. Zhao²², N. Zhigareva⁵⁸, D. Zhou⁷, Y. Zhou^{80,57}, Z. Zhou¹⁸, H. Zhu^{18,7}, J. Zhu^{7,113}, X. Zhu⁷, A. Zichichi^{28,12}, A. Zimmermann⁹³, M.B. Zimmermann^{36,54}, G. Zinovjev³, M. Zyzak⁴³

Affiliation notes

ⁱ Deceased

ⁱⁱ Also at: M.V. Lomonosov Moscow State University, D.V. Skobeltsyn Institute of Nuclear Physics, Moscow, Russia

ⁱⁱⁱ Also at: University of Kansas, Lawrence, Kansas, United States

Collaboration Institutes

¹ A.I. Alikhanyan National Science Laboratory (Yerevan Physics Institute) Foundation, Yerevan, Armenia

² Benemérita Universidad Autónoma de Puebla, Puebla, Mexico

³ Bogolyubov Institute for Theoretical Physics, Kiev, Ukraine

⁴ Bose Institute, Department of Physics and Centre for Astroparticle Physics and Space Science (CAPSS), Kolkata, India

⁵ Budker Institute for Nuclear Physics, Novosibirsk, Russia

⁶ California Polytechnic State University, San Luis Obispo, California, United States

⁷ Central China Normal University, Wuhan, China

⁸ Centre de Calcul de l'IN2P3, Villeurbanne, France

⁹ Centro de Aplicaciones Tecnológicas y Desarrollo Nuclear (CEADEN), Havana, Cuba

¹⁰ Centro de Investigaciones Energéticas Medioambientales y Tecnológicas (CIEMAT), Madrid, Spain

- 11 Centro de Investigación y de Estudios Avanzados (CINVESTAV), Mexico City and Mérida, Mexico
- 12 Centro Fermi - Museo Storico della Fisica e Centro Studi e Ricerche “Enrico Fermi”, Rome, Italy
- 13 Chicago State University, Chicago, Illinois, USA
- 14 China Institute of Atomic Energy, Beijing, China
- 15 Commissariat à l’Energie Atomique, IRFU, Saclay, France
- 16 COMSATS Institute of Information Technology (CIIT), Islamabad, Pakistan
- 17 Departamento de Física de Partículas and IGFAE, Universidad de Santiago de Compostela, Santiago de Compostela, Spain
- 18 Department of Physics and Technology, University of Bergen, Bergen, Norway
- 19 Department of Physics, Aligarh Muslim University, Aligarh, India
- 20 Department of Physics, Ohio State University, Columbus, Ohio, United States
- 21 Department of Physics, Sejong University, Seoul, South Korea
- 22 Department of Physics, University of Oslo, Oslo, Norway
- 23 Dipartimento di Elettrotecnica ed Elettronica del Politecnico, Bari, Italy
- 24 Dipartimento di Fisica dell’Università ‘La Sapienza’ and Sezione INFN Rome, Italy
- 25 Dipartimento di Fisica dell’Università and Sezione INFN, Cagliari, Italy
- 26 Dipartimento di Fisica dell’Università and Sezione INFN, Trieste, Italy
- 27 Dipartimento di Fisica dell’Università and Sezione INFN, Turin, Italy
- 28 Dipartimento di Fisica e Astronomia dell’Università and Sezione INFN, Bologna, Italy
- 29 Dipartimento di Fisica e Astronomia dell’Università and Sezione INFN, Catania, Italy
- 30 Dipartimento di Fisica e Astronomia dell’Università and Sezione INFN, Padova, Italy
- 31 Dipartimento di Fisica ‘E.R. Caianiello’ dell’Università and Gruppo Collegato INFN, Salerno, Italy
- 32 Dipartimento di Scienze e Innovazione Tecnologica dell’Università del Piemonte Orientale and Gruppo Collegato INFN, Alessandria, Italy
- 33 Dipartimento Interateneo di Fisica ‘M. Merlin’ and Sezione INFN, Bari, Italy
- 34 Division of Experimental High Energy Physics, University of Lund, Lund, Sweden
- 35 Eberhard Karls Universität Tübingen, Tübingen, Germany
- 36 European Organization for Nuclear Research (CERN), Geneva, Switzerland
- 37 Excellence Cluster Universe, Technische Universität München, Munich, Germany
- 38 Faculty of Engineering, Bergen University College, Bergen, Norway
- 39 Faculty of Mathematics, Physics and Informatics, Comenius University, Bratislava, Slovakia
- 40 Faculty of Nuclear Sciences and Physical Engineering, Czech Technical University in Prague, Prague, Czech Republic
- 41 Faculty of Science, P.J. Šafárik University, Košice, Slovakia
- 42 Faculty of Technology, Buskerud and Vestfold University College, Vestfold, Norway
- 43 Frankfurt Institute for Advanced Studies, Johann Wolfgang Goethe-Universität Frankfurt, Frankfurt, Germany
- 44 Gangneung-Wonju National University, Gangneung, South Korea
- 45 Gauhati University, Department of Physics, Guwahati, India
- 46 Helsinki Institute of Physics (HIP), Helsinki, Finland
- 47 Hiroshima University, Hiroshima, Japan
- 48 Indian Institute of Technology Bombay (IIT), Mumbai, India
- 49 Indian Institute of Technology Indore, Indore (IITI), India
- 50 Inha University, Incheon, South Korea
- 51 Institut de Physique Nucléaire d’Orsay (IPNO), Université Paris-Sud, CNRS-IN2P3, Orsay, France
- 52 Institut für Informatik, Johann Wolfgang Goethe-Universität Frankfurt, Frankfurt, Germany
- 53 Institut für Kernphysik, Johann Wolfgang Goethe-Universität Frankfurt, Frankfurt, Germany
- 54 Institut für Kernphysik, Westfälische Wilhelms-Universität Münster, Münster, Germany
- 55 Institut Pluridisciplinaire Hubert Curien (IPHC), Université de Strasbourg, CNRS-IN2P3, Strasbourg, France
- 56 Institute for Nuclear Research, Academy of Sciences, Moscow, Russia
- 57 Institute for Subatomic Physics of Utrecht University, Utrecht, Netherlands
- 58 Institute for Theoretical and Experimental Physics, Moscow, Russia
- 59 Institute of Experimental Physics, Slovak Academy of Sciences, Košice, Slovakia
- 60 Institute of Physics, Academy of Sciences of the Czech Republic, Prague, Czech Republic
- 61 Institute of Physics, Bhubaneswar, India

- 62 Institute of Space Science (ISS), Bucharest, Romania
- 63 Instituto de Ciencias Nucleares, Universidad Nacional Autónoma de México, Mexico City, Mexico
- 64 Instituto de Física, Universidad Nacional Autónoma de México, Mexico City, Mexico
- 65 iThemba LABS, National Research Foundation, Somerset West, South Africa
- 66 Joint Institute for Nuclear Research (JINR), Dubna, Russia
- 67 Konkuk University, Seoul, South Korea
- 68 Korea Institute of Science and Technology Information, Daejeon, South Korea
- 69 KTO Karatay University, Konya, Turkey
- 70 Laboratoire de Physique Corpusculaire (LPC), Clermont Université, Université Blaise Pascal, CNRS–IN2P3, Clermont-Ferrand, France
- 71 Laboratoire de Physique Subatomique et de Cosmologie, Université Grenoble-Alpes, CNRS-IN2P3, Grenoble, France
- 72 Laboratori Nazionali di Frascati, INFN, Frascati, Italy
- 73 Laboratori Nazionali di Legnaro, INFN, Legnaro, Italy
- 74 Lawrence Berkeley National Laboratory, Berkeley, California, United States
- 75 Lawrence Livermore National Laboratory, Livermore, California, United States
- 76 Moscow Engineering Physics Institute, Moscow, Russia
- 77 National Centre for Nuclear Studies, Warsaw, Poland
- 78 National Institute for Physics and Nuclear Engineering, Bucharest, Romania
- 79 National Institute of Science Education and Research, Bhubaneswar, India
- 80 Niels Bohr Institute, University of Copenhagen, Copenhagen, Denmark
- 81 Nikhef, Nationaal instituut voor subatomaire fysica, Amsterdam, Netherlands
- 82 Nuclear Physics Group, STFC Daresbury Laboratory, Daresbury, United Kingdom
- 83 Nuclear Physics Institute, Academy of Sciences of the Czech Republic, Řež u Prahy, Czech Republic
- 84 Oak Ridge National Laboratory, Oak Ridge, Tennessee, United States
- 85 Petersburg Nuclear Physics Institute, Gatchina, Russia
- 86 Physics Department, Creighton University, Omaha, Nebraska, United States
- 87 Physics Department, Panjab University, Chandigarh, India
- 88 Physics Department, University of Athens, Athens, Greece
- 89 Physics Department, University of Cape Town, Cape Town, South Africa
- 90 Physics Department, University of Jammu, Jammu, India
- 91 Physics Department, University of Rajasthan, Jaipur, India
- 92 Physik Department, Technische Universität München, Munich, Germany
- 93 Physikalisches Institut, Ruprecht-Karls-Universität Heidelberg, Heidelberg, Germany
- 94 Politecnico di Torino, Turin, Italy
- 95 Purdue University, West Lafayette, Indiana, United States
- 96 Pusan National University, Pusan, South Korea
- 97 Research Division and ExtreMe Matter Institute EMMI, GSI Helmholtzzentrum für Schwerionenforschung, Darmstadt, Germany
- 98 Rudjer Bošković Institute, Zagreb, Croatia
- 99 Russian Federal Nuclear Center (VNIIEF), Sarov, Russia
- 100 Russian Research Centre Kurchatov Institute, Moscow, Russia
- 101 Saha Institute of Nuclear Physics, Kolkata, India
- 102 School of Physics and Astronomy, University of Birmingham, Birmingham, United Kingdom
- 103 Sección Física, Departamento de Ciencias, Pontificia Universidad Católica del Perú, Lima, Peru
- 104 Sezione INFN, Bari, Italy
- 105 Sezione INFN, Bologna, Italy
- 106 Sezione INFN, Cagliari, Italy
- 107 Sezione INFN, Catania, Italy
- 108 Sezione INFN, Padova, Italy
- 109 Sezione INFN, Rome, Italy
- 110 Sezione INFN, Trieste, Italy
- 111 Sezione INFN, Turin, Italy
- 112 SSC IHEP of NRC Kurchatov institute, Protvino, Russia
- 113 SUBATECH, Ecole des Mines de Nantes, Université de Nantes, CNRS-IN2P3, Nantes, France
- 114 Suranaree University of Technology, Nakhon Ratchasima, Thailand

- 115 Technical University of Košice, Košice, Slovakia
- 116 Technical University of Split FESB, Split, Croatia
- 117 The Henryk Niewodniczanski Institute of Nuclear Physics, Polish Academy of Sciences, Cracow, Poland
- 118 The University of Texas at Austin, Physics Department, Austin, Texas, USA
- 119 Universidad Autónoma de Sinaloa, Culiacán, Mexico
- 120 Universidade de São Paulo (USP), São Paulo, Brazil
- 121 Universidade Estadual de Campinas (UNICAMP), Campinas, Brazil
- 122 University of Houston, Houston, Texas, United States
- 123 University of Jyväskylä, Jyväskylä, Finland
- 124 University of Liverpool, Liverpool, United Kingdom
- 125 University of Tennessee, Knoxville, Tennessee, United States
- 126 University of the Witwatersrand, Johannesburg, South Africa
- 127 University of Tokyo, Tokyo, Japan
- 128 University of Tsukuba, Tsukuba, Japan
- 129 University of Zagreb, Zagreb, Croatia
- 130 Université de Lyon, Université Lyon 1, CNRS/IN2P3, IPN-Lyon, Villeurbanne, France
- 131 V. Fock Institute for Physics, St. Petersburg State University, St. Petersburg, Russia
- 132 Variable Energy Cyclotron Centre, Kolkata, India
- 133 Warsaw University of Technology, Warsaw, Poland
- 134 Wayne State University, Detroit, Michigan, United States
- 135 Wigner Research Centre for Physics, Hungarian Academy of Sciences, Budapest, Hungary
- 136 Yale University, New Haven, Connecticut, United States
- 137 Yonsei University, Seoul, South Korea
- 138 Zentrum für Technologietransfer und Telekommunikation (ZTT), Fachhochschule Worms, Worms, Germany